UNIVERSITY
OF
KWAZULU-NATAL

Effect of ADLash Optical Fibre Cable on Corona Onset Gradient and Electric Fields around the Shield Wire of the Apollo-Cahora Bassa HVDC Line

By

Eamon Riccardo Bussy
NTD, GCC, Dip Dat

Dissertation submitted in partial fulfilment of the requirements for the degree of
Master of Science Degree in Power and Energy Systems
for the University of KwaZulu-Natal.

The author hereby declares that this dissertation represents his own work, except where other authors' works have been used, in which case the use thereof is referenced.

Eamon Riccardo Bussy   14 March 2005
Dissertation Author   Date

Supervisors:

- **Prof. N. M. Ijumba**
  Pr Eng, C Eng, BSc (Eng)(Hons), MSc, PhD

- **Prof. A C. Britten**
  Pr Eng, BSc (Eng), MSc (Eng)

Dedication

This dissertation is dedicated ...

To Christine, my wife
The love of my life
Who supports me all the way;

To Nicole, my big girl
My big hearted first born
Who worries when I get stressed;

To Danielle, my cuddly girl
Always there with a hug or a kiss
Who knows when I work I need tea;

To Bernard, my young apprentice
My junior handyman
Who also wants to be an Engineer;

To all of my family: big and small
Who love me as I love them;
I love them all.

One of the hardest things in the world
is to convey a meaning
accurately from one mind to another.

Life and Letters: Lewis Carroll

Acknowledgements

Several people have helped me in the work described in this dissertation. I am grateful to them and wish to thank them for their contribution.

- Anand Singh the HVDC laboratory technician who patiently helped me with all the tests;

- Durban Institute of Technology for the loan of some high voltage equipment;

- Gary Sibilant for supplying technical information from ESKOM, especially that of the HVDC line;

- Leena Rajpal for providing administrative support and encouragement;

- Rob Phillips of Aberdare for providing the ADLash specifications; and

- THRIP and ESKOM who have provided research funding to make this possible

Abstract

ADLash® is the trade name for an optical fibre cable attached to a transmission line shield wire using aramid-reinforced bands. The installation of this type of optic fibre cable has been considered for the HVDC line from the Songo hydroelectric scheme at Cahora Bassa in Moçambique, to Apollo substation in South Africa. The impact that installation of this cable will have on the onset of corona is examined.

The shield wire with and without ADLash attached is modelled for both the actual line configuration and for corona cage studies. The electric field is calculated using the Method of Images and the Boundary Element Method to predict the electric field enhancements and to estimate the corona onset gradient.

Corona onset gradients and phenomena for smooth and stranded conductors are researched to aid the prediction of voltage onset magnitudes for the corona cage. Estimated values are compared with observed values for both AC and DC applied voltages. Different patterns of corona and different corona onset voltages are observed for AC and negative DC applied voltages.

The relative permittivity of the ADLash is higher than the surrounding air and this is shown to lead to greatly enhanced electric fields at the air/ dielectric/ shield wire interfaces that are significant enough to cause corona at the rated operating voltage. The corona will bombard the ADLash and probably damage it.

Some alternative methods of installing fibre optic cables are reviewed for further research because the use of ADLash cannot be recommended.

Contents

List of Tables

List of Figures

List of Abbreviations

Aberdare	Aberdare Cables (Pty) Ltd.
ACSR	aluminium conductor with steel reinforcing
ADLash	all-dielectric fibre optic cable, externally lashed to a conductor using bands
ADSS	All dielectric self supporting optic fibre cable
ASU	Arizona State University
band	AD-Lashing band used to tape the ADLash to the conductor wire
BEM	Boundary element method
cage	corona cage
HVDC	high voltage direct current (Apollo-Cahora Bassa line unless otherwise specified)
IEEE	Institution of Electrical and Electronic Engineers
MI	Method of images
OPGW	Optical ground wire
PLC	power line carrier
STP	Standard atmospheric temperature and pressure
UKZN	University of Kwazulu-Natal
+ve	positive
-ve	negative
WRAP	Helically-applied Fibre-optic cable
WSU	Washington State University

List of Symbols

α	first ionisation coefficient
γ	second ionisation coefficient
δ	air density factor
ϵ	absolute permittivity
ϵ_0	permittivity of free space ($4\pi \cdot 10^{-7}$ Hm^{-1})
ϵ_r	relative permittivity
η	attachment coefficient
a, b	calculation symbols
C	capacitance
D_b	main conductor bundle diagonal distance between conductor centres
d_c	main conductor diameter
d_f	field inhomogeniety (or field divergency) factor
d_s	diameter of the centres of the outer strands of the shield wire
f	frequency
f_{ADL}	stress enhancement factor – with ADLash
f_{air}	stress enhancement factor – no ADLash
G	electric field strength $\left(\frac{dV}{dx}\right)$
G_{ave}	average surface stress
G_c	conductor surface electric field strength, value at corona onset
$G_{max, MR, MA, MSA}$	peak value of surface stress for various calculations
G_{sw}	onset stress of shield wire
h_e	height of the centre of the shield wire
i, j	calculation counters
I	current

I_0	current at ionisation threshold
L	inductance
m	stranded conductor surface factor
N^*	number of free electrons (≈ 3500) that transforms an avalanche into a self propagating streamer
N_0	number of free electrons at ionisation limit
N_c	number of free electrons on conductor surface
n, N	number free electrons due to ionisation
P	horizontal spacing between centres of main conductor and shield wire
q	electric charge
q_c	average shield wire charge per conductor
q_s	average shield wire charge
r	radius
R	concentric cylinder outer radius; corona cage outer radius, also electrical resistance as applicable
r_c	conductor radius
r_o	radius of ionisation limit
S_c	main conductor bundle spacing
V	voltage
V_c	conductor voltage
$V_{A, R, STR, SA}$	onset voltage of bare stranded shield wire for different calculations
V_S	corrected sphere flash-over voltage
V_{table}	average observed sphere flash-over voltage
X	positive or negative ion

Chapter 1 Introduction

As a world wide trend, many electric utilities are fitting high capacity fibre optic cables to high voltage transmission lines to improve their own communication needs. Where digital fault protection systems have been introduced, fibre optic cables easily provide for the greater bandwidth demand and have the added advantage of being immune to electromagnetic interference. The utilities are also able to take advantage of the additional revenues that can be gained by leasing excess capacity for other telecommunication purposes. However, when fibre optic cables are fitted to high voltage transmission lines, some technical and safety-related challenges occur [1].

Many of Eskom's overhead transmission lines have already been fitted with optic fibre cables for the advantages listed above. One line not yet fitted with optic fibre cables is the existing Apollo - Cahora Bassa high voltage DC (HVDC) line which delivers a maximum of 1 760 MW of power at 533 kV DC over a distance of 1 414 km from Moçambique to South Africa [2]. Reliable internal communications are vital to ensure protection and control of this power supply for stable operation. At present a power line carrier system (PLC) is used which superimposes a high frequency signal on the line for communication, operation, and control purposes. It has been found that the PLC is limited in bandwidth. When corona (which is worse on the negative line during wet weather) occurs, the PLC suffers from reduced signal-to-noise ratios. In addition the HVDC line compromises PLC communications when faults occur [3].

According to Jones, the types of optic cable suitable for overhead transmission lines can be grouped into three broad categories [4]. Optical fibres can be encased within the ground or shield

wire (OPGW), they can be wrapped around (WRAP) a conductor, or they can be contained in an all-dielectric self-supporting (ADSS) cable. Not listed is the type where the fibre optic cable is lashed to an existing conductor using bands (ADLash[1]) which is an installation that is similar to, but not the same as WRAP.

Of the types available, ADLash optical fibre cable has been considered for retrofitting to the existing shield wire of the HVDC line to provide a telecommunications medium. The cost of undertaking this is high and needs to be fully investigated before implementation. This dissertation examines the effect of ADLash on the electric fields and corona onset gradient around the shield wire. The results will help designers to predict the effects of installing ADLash on the HVDC line.

1.1   Problem Description

The main conductor of the HVDC line will often have corona around it depending on factors such as voltage level, polarity, weather, and surface condition of the conductors [5]. The shield wire is at a much lower voltage (approximately at earth potential) but could still experience corona due to the electric field strength on its surface. With the original design, corona around the shield conductor was not of much concern, but if ADLash is taped to the shield wire, any corona that may occur will bombard the ADLash cable sheath eventually damaging it by puncturing the outer sheath and allowing moisture ingress. This damage will be similar to the failure phenomena seen on aging non-ceramic insulators [6] and similar to damage observed on ADSS fibre optic cables which has been reported in several publications including [7] and [8].

---

[1]ADLash is a registered trademark of Aberdare Cables Pty (Ltd)

The research for this dissertation was conducted to answer the following questions:

- Under what conditions does corona occur and under what conditions could it be present on the HVDC shield wire?

- What methods are suitable for modelling the electric field around the shield wire?

- What effect will ADLash have on the electric field in the immediate vicinity of the shield wire surface?

- If ADLash is fitted to the shield wire, is it likely to aggravate the incidence of corona?

- Can the effects of the ADLash be observed in a corona cage?

- Apart from the effects of the introduction of ADLash, what other sources of partial breakdown are there which can lead to corona?

- If ADLash is not suitable, would the other fibre optic cable technologies be suitable?

At the completion of this dissertation, Eskom will have a better understanding of the electric fields surrounding the shield wire with and without ADLash. They will also have an idea of the suitability or otherwise of ADLash for the HVDC line and of alternatives available for further investigation.

Chapter 2   Procedure Followed and Materials Used

In this chapter the procedure in carrying out this dissertation is briefly summarised. In addition the materials used, are listed.

2.1   Research for Suitable Information Sources

Information sources had to be found which provided information in five broad areas. A brief overview of these is provided in the next chapter.

2.2   HVDC Line Conductor Configuration

The HVDC line consists of a shield wire nominally 10.9 m higher than the conductor bundle. The horizontal distance between the centres of the shield wire and the conductor bundle is 3.6 m, while the vertical distance is 10.9 m, which gives a distance of 11.48 m between the centres. Refer to Appendix A for further details.

The respective maximum heights of the shield wire and conductor bundle are 36.7 m and 25.8 m at the towers. The line has a sag of 16 m midway between the towers, yielding minimum heights of 20.7 m and 9.8 m respectively [9].

2.3   HVDC Shield Wire Description

The shield wire conductor similar to Figure 2.1, is manufactured by Aberdare Cables (Pty.) Ltd., (Aberdare). It is an aluminium conductor with steel reinforcing (ACSR) and is designated "Oden:

Figure: 2.1   ACSR 12/7 3.52   (*Aberdare*)

12/7/3.52" which consists of a core of seven steel wires surrounded by twelve aluminium wires. All strands have a diameter of 3.52 mm. The overall conductor diameter is 17.6 mm. Further details are available in Appendix B. The surface stress on the outer strands is examined with and without ADLash.

2.4   Main Conductor Bundle Description

The main conductor bundle comprises four conductors in a horizontal square as illustrated in Figure 2.2. The conductors have an outer diameter of 31.8 mm and are spaced at 450 mm. They are also manufactured by Aberdare and are designated 'Zambezi: 42/4.14 + 7/2.32', having forty-two aluminium strands of 4.14 mm diameter surrounding a steel core of seven strands of 2.32 mm diameter. Further details of the conductors are given in Appendix C. The outer layer has twenty-one aluminium strands.
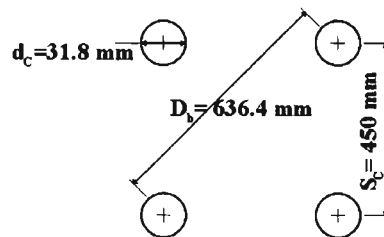
Figure 2.2   HVDC Main Conductor Bundle

2.5   Description of ADLash

ADLash is an externally attached 24 optical fibre cable manufactured to meet Eskom specification, TSP0319. For this dissertation a sample of '24 fi 3*8 LASH / 01' ADLash was supplied by Aberdare Cables. Refer to Appendix D for the specification sheet.
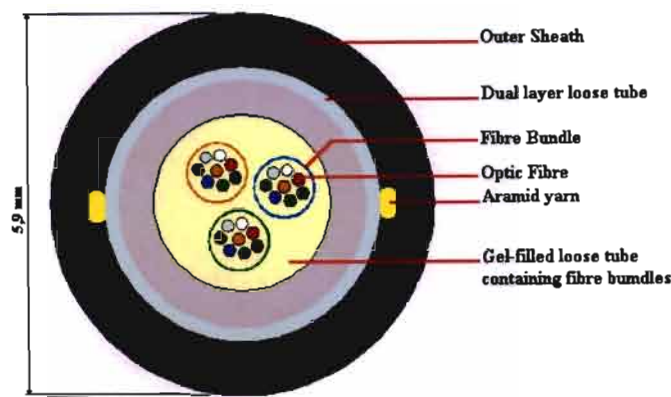
Figure 2.3   ADLash Cross Section   *(Aberdare)*

ADLash consists of three fibre bundles each containing eight fibres as shown in Figure 2.3. The bundles are embedded in a dual layer polycarbonate/ polyethylene tube with a gel compound. This is all covered with a medium density polyethylene sheath. Longitudinal strength is achieved by means of aramid yarns. The nominal diameter is 5.9 mm.

Table: 2.1   Permittivity of ADLash Layers

Layer	Permittivity	Source
Optical Fibre	5	Corning
Loose tube - Gel filled	4	Aberdare
Dual layer - Inner layer	3	Aberdare
Dual layer - Outer layer	2.3	Aberdare
Aramid yarn	4	Assumed
Outer sheath	2.55	Aberdare

The permittivity values of the various layers, as supplied by Aberdare Cables, are given in Table 2.1.Where the permittivity is not available, an intermediate value is assumed between the given values to avoid unacceptable distortions of the stress.

2.6   AD-Lashing Band Description

The ADLash band (band) is used to bind the ADLash to the shield wire. It is retrofitted to existing lines using a custom-made machine [10]. As illustrated in Figure 2.4, the bands are made up of
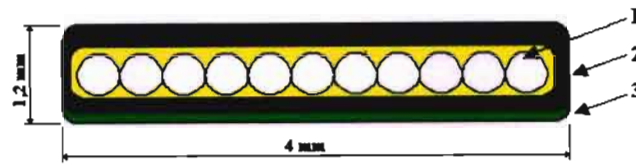
Figure: 2.4   AdLash Band   (*Aberdare*)

glass yarns, 1, embedded in melt glue jacketed with a cross-linked polyethylene sheath, 2, with

an anti-skid layer, 3, for shock resistance. More details are available in Appendix E.

2.7   The Corona Discharge

To examine the possibility of corona onset on the shield wire, the mechanisms and characteristics

of corona discharges in air are presented and the conditions leading to corona onset are described.

Ways of predicting corona onset in air have been reported by various researchers over the last

century and some of their methods are examined and compared. These methods are used to

predict the onset of corona around an aluminium rod and around a sample of shield wire in the

corona cage at the HVDC laboratory at UKZN.

2.8   HVDC Shield Wire Surface Gradient

The HVDC line is modelled using the Method of Images (MI) and using the Boundary Element

Method (BEM). The latter being used to plot the electric field surface stress on the shield wire

with, and without, ADLash attached. Areas of maximum stress are identified and evaluated to see

if partial break down is likely.

2.9   Corona Cage Simulations and Corona Cage Tests

Models of samples of smooth aluminium rod and stranded shield wire in a concentric cylinder configuration are done with BEM to simulate the corona cage to be compared with actual HVDC laboratory tests. Areas of maximum stress are identified and evaluated to see if partial break down is likely.

After checking the calibration of the HVDC supply, results of tests are with a corona cage are presented to be compared with the theoretical estimates of corona onset.

First two stranded conductors are arranged in a quasi-parallel configuration to demonstrate that corona first starts on the negative conductor as the voltage is slowly increased

Corona onset in the corona cage is then observed for an aluminium rod and for a sample of shield wire with and without ADLash attached.

2.10   Other Sources of Partial Breakdown

Research on possible corona sources (other than those simply due to the electric field surrounding the shield wire with and without the ADLash) are presented with comment on the possible relevance to this dissertation is presented.

2.11   Alternative Fibre Optic Cable Technologies

Some other optic fibre installation technologies are reviewed and their suitability as alternatives

to ADLash are examined.

2.12   Units Used

Metric units are used throughout. Electric stress values are recorded in kilovolts per centimetre [$kVcm^{-1}$] as is customary. In all instances where standard metric units are not used, the applicable units are clearly given.

2.13   Results and Conclusions

Results of the dissertation are presented concisely and then suitable conclusions are drawn.

Data and calculations that are too bulky are placed in appendices at the back together with manufacturer specification sheets and may be referred to for further information.

Chapter 3   Overview of Literature Sources

Extensive literature reviewing has been done at the commencement of this dissertation and continued throughout. Extensive use was made of the libraries of Durban Institute of Technology, the University of KwaZulu-Natal, and ESKOM research centre. The Internet has also been a useful source and extensive searches were undertaken for relevant information. Searches were mainly directed in the following areas:

- Electrostatic theory and field plotting

- Corona phenomena

- High voltage measurements

- Information on optic fibre cable technology

- Cahora-Bassa/ Apollo HVDC line parameters

Information used, is from textbooks and published articles. Where possible more than one reference has been obtained to ensure accuracy of information. Where the information is identical, only one reference is made. A brief overview of the literature obtained is given here without page references. The full details of literature used, are cited in the references to the main text.

3.1   Electrostatic Theory and Field Plotting

Electrostatic and electric field theory has been studied so that an understanding could be obtained of the methods used for calculating electric stresses and potentials in the space surrounding conductors.

Main sources used are:

- 'Electric Power Research Institute (EPRI) HVDC Transmission Line Reference Book' [11]

- 'High Voltage Engineering' by I. Khalifa [12] for calculations based on the 'Method of Images'.

- 'High Voltage Engineering Fundamentals' by E. Kuffel, W. F. Zaengl, and J. Kuffel, [13] provided information on 'Boundary Element Analysis'.

3.2   Corona Phenomena

To get a good understanding of corona onset and its phenomena the following texts are referred to:

- 'Dielectric Phenomena in High Voltage Engineering' by F. W. Peek [14]

- 'Electrical Breakdown and Discharges in Gases' by E. E. Kunhardt and L. H. Luessen, [15]

- 'Gaseous Conductors' by J. D. Cobine [16]

- 'Electrical Corona' by L. B. Loeb [17]

- 'Corona Onset Criterion' by D. B. Phillips [18]

- 'The Lightning Flash' by V. Cooray [19]

Literature reviewed included observations on concentric smooth cylindrical conductors, parallel wires, and point-cup configurations. None of the publications surveyed considered corona observed on stranded conductors in any detail other than suggesting stranding factors to modify calculations for smooth cylindrical conductors, which appears to be an unfortunate omission

given the extensive use of these conductors.

3.3   High Voltage Measurements

High Voltage measurements were calibrated in accordance with, IEEE Standard Techniques for High-Voltage Testing (IEEE Std-1978) [20].

3.4   Information on Fibre Optic Cable Technology

The following literature provided information on fibre optic cables:

- Aberdare Fibre Optic Cable information sheet (see Appendix: E)

- 'Fibre Optic Cables in Overhead Transmission Corridors: A State-of-the-Art Review', by J. A. Jones [21]

- Various university publications and publications from the Institute of Electrical and Electronic Engineers (IEEE), which are referenced in detail in the text where they are used

Much information is available on All Dielectric Self-Supporting fibre optic cable (ADSS), but it seems that very little has been published on ADLash fibre optic cables. Only the first two publications listed above contained relevant information, the first merely being a specification sheet.

3.5   Cahora-Bassa/ Apollo HVDC Line Layout

Details of the pylon structures, line heights, line voltages, altitudes and other relevant information were provided by G. Sibilant of Technology Services International, Eskom.

3.6   General

The references mentioned here are the ones that had more importance for the successful completion of this dissertation. A brief survey of all the references at the end of the text will show that there are too many to mention individually in this chapter. Their use is inherently clear in the text and the citations include page numbers to simplify locating pertinent information in the relevant articles.

Chapter 4   Corona Onset in Concentric Cylinders

To understand the effects of voltage applied to the HVDC line, it is necessary to first understand

the basic processes of the partial breakdown that causes the corona around the conductor surfaces

when the applied voltage exceeds its onset value. Different phenomena are seen depending on the

conductor surface, electric field stresses, the polarity, the space charge, etcetera.

The following descriptions have been compiled from the literature listed in Chapter 3.2. Much

of the information presented is common to all these texts, so citations are only given where

strictly necessary.

4.1   The Corona Discharge

Consider two electrodes with voltage applied to them with ultraviolet light directed at them. As
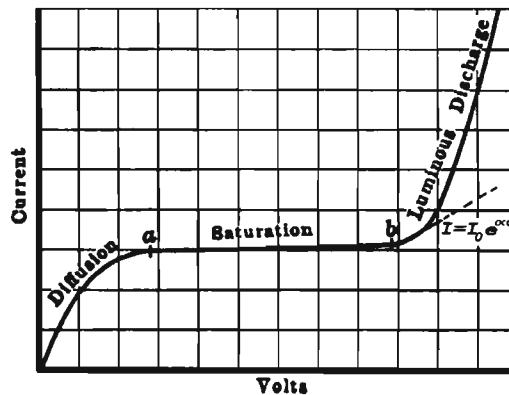
Figure: 4.1   Average Current Growth as a Function of Applied Voltage   *(Peek)*

the voltage is increased, the current increases with voltage up to point *a*, as shown in Figure 4.1.

Between '*a*' and '*b*' the current is hardly affected by an increase in voltage, although it may be

noticeably increased by increasing the intensity of the ultraviolet radiation [22]. It may be

concluded that the current between *a* and *b* is primarily a photoelectric current produced at the

cathode by the ultraviolet radiation. As the voltage increases beyond *b*, the current increase is initially attributed to ionisation by collision, while secondary ionisation processes are used to explain the sharper increase of the curve up to the point of breakdown [23]. The luminous discharge is called *corona* if it does not extend from one electrode to the other and it is called *breakdown* if the gap between the conductors is bridged.

Corona, (from the word *couronne* - being french for crown, an example of which is shown in Figure 4.2, [24]), is "...used to describe the general class of luminous phenomena appearing associated with the current jump to some micro-amperes at the highly stressed electrode..." [25]. The current value at the jump (at point *b*), together with the applied voltage value define the corona threshold, and usually just precede the initial appearance of corona.

Corona may be defined as "...a self-sustained electrical discharge where the Laplacian
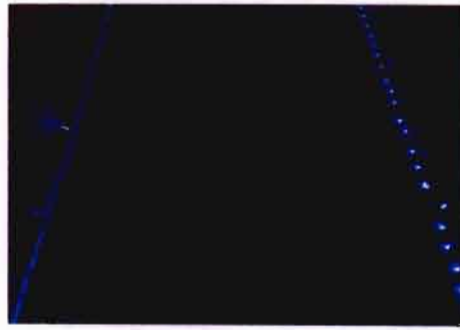
Figure 4.2   Positive Corona (Left), and Negative Corona (Right), on Parallel Wires   [*WSU*]

(geometrically determined) electric field confines the primary ionisation processes to regions close to high-field electrodes or insulators." [26]. The actual electric field may however be somewhat distorted by space charges.

The visible corona is evidence of electromagnetic radiation that is primarily in the ultraviolet/ visual range. This in turn is due to radiative recombination [27], where a positive ion X^+ combines with an electron e^- resulting in an excited neutral atom X^* and the release of

electromagnetic radiation in the form of a photon having energy $W = hf$ described as follows:

$$X^+ + e^- \rightarrow X^* + hf \qquad (4.1)$$
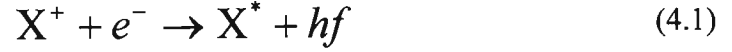
where $h = 6.626 \cdot 10^{-34}$ Js, Planck's constant and f is the radiation frequency.

Corona may also be seen where attachment processes are seen as described later in Chapter 4.9.

4.2   Corona Discharges in Air

Different modes of corona around a conductor can be seen depending on polarity and magnitude of applied voltage, as well as whether the applied voltage is AC or DC. Where the electric field is non-uniform, as in a concentric cylinder configuration, corona first commences at the highly stressed electrode and increases in size and intensity until breakdown is initiated.

When the corona onset conditions are met for a plane uniform gap, where the electric field is uniform across the gap, these onset conditions will be applicable for the entire gap. So corona onset will always be accompanied by breakdown. References to corona in this dissertation apply to non-uniform airgaps where corona occurs at the highly stressed electrodes.

4.3   Positive Conductor Corona Characteristics

The phenomena associated with corona depend on the polarity of the electrode under consideration. The following characteristics may be noted for a positive conductor [28].

Burst corona, in the form of a velvet type of glow will first be seen on the centre conductor in the

cylindrical cylinder configuration when the corona has just started, together with an intermittent current.

As the stress and current increase slightly, the glow spreads along the conductor and into the gap for a millimetre or so when pre-onset streamers appear.

Once the corona is established slightly beyond the pre-streamer potential, the conductor is surrounded by a smooth blue-white glow that is a glow discharge influenced by negative space charge due to electronic attachment, which suppresses the streamers. This current associated with this glow is continuous but fluctuating and the glow only develops in the presence of negative ions [29].

At very high potentials, just below spark breakdown, highly luminous streamers extend into the gap, particularly where the centre conductor radius r_c is much less than the outer cylinder radius R.

4.4   Negative Conductor Corona Characteristics

For a highly stressed negative electrode, the luminosity occurs in reddish tufts or beads that are intermittent localised glow discharges of diameter of about 0.02 cm. First one spot will appear and then further spots will be seen along the length of the electrode. The current is seen to flow in very regular pulses and are called Trichel pulses. The onset voltage is close to the value of voltage associated with the onset of streamers under positive voltage.

At a much higher voltage a steady glow is seen although the transition from the pulses to the glow is not sharply defined.

4.5   The Concentric Cylinder Configuration

The concentric cylinder configuration is depicted in Figure 4.3 and it illustrates an example of a

corona discharge system that consists of the centre conductor of radius r_c that is highly stressed,
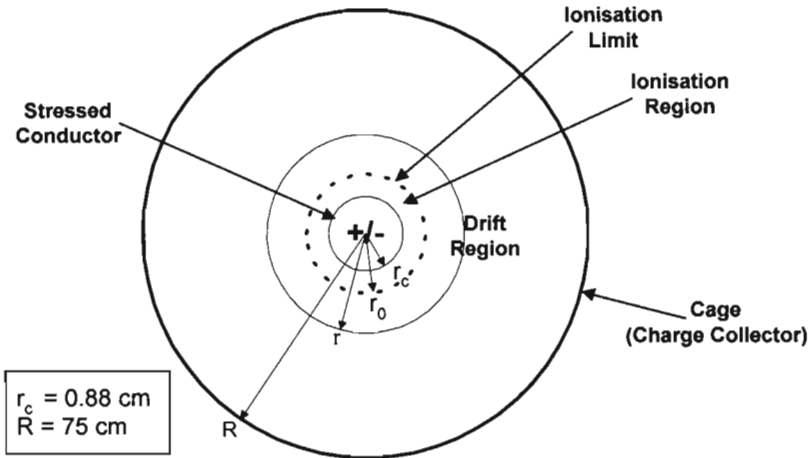
Figure 4.3   Concentric Cylinder Configuration

surrounded by an ionisation region from r_c to r_0 where free charges are produced. The relatively

lower stress region from r_0 to R is called the drift region. The outer cage R mainly acts as a charge

collector. The value of the field G_x at any radius x may be calculated knowing the dimensions of

r and R and also the applied voltage V, using Equation (2.1) [30].

$$G_r = \frac{V}{r \ln \dfrac{R}{r_c}}   \; [\text{kVcm}^{-1}]$$ (4.1)

4.6   Ionisation by Collision

The basic corner stone of all corona is Townsend's description of an electronic avalanche. This

explanation neglects the effects of field distortions due to space charge. Consider two parallel

electrodes as shown in Figure 4.4(a), [31]. A voltage V applied between the anode and cathode

-18-

will cause an electric field of $G = V/d$ to be set up between the plates. Any electrons between the
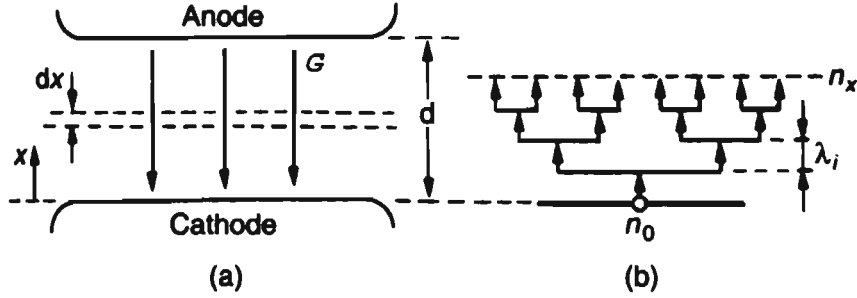
Figure 4.4   Sketch of Electron Multiplication Gap Arrangement **(a)**, and Electron Avalanche **(b)**   (*Kuffel et al*)

plates will be accelerated toward the anode. If n_0 electrons leave the cathode, they will accelerate

toward the anode. Where they have kinetic energy at least equal to the ionisation potential λ_i of

the atoms between the electrodes, they will cause ionising collisions during which electrons will

be liberated from the atoms that will become positive ions. The electrons will continue toward

the anode, having more collisions along the leading to an avalanche as depicted in Figure 4.4 (b),

while the positive ions will accelerate toward the cathode. When the electrons have travelled a

distance of x after more collisions, the number of electrons will be n_x. When these electrons have

travelled a slightly further distance of dx they create $\alpha\, n_x\, dx$ electrons where α, the average

number of electron ionising collisions per unit travel is called 'Townsend's first ionising

coefficient' and hence $dn_x = \alpha\, n_x\, dx$. Solution of this equation from $x = 0$ to $x = d$ leads to

$n_d = n_0\, e^{\alpha d}$. Since electron movement represents current, the average current in the gap may be

expressed as $I = I\, e^{\alpha d}$, as illustrated in Figure 4.1.

4.7   Current Growth due to Secondary Processes

When the applied voltage is further increased, secondary ionising processes occur and the

'secondary ionising coefficient γ' is defined as the average number of secondary electrons

produced per incident ion, photon, excited particle or metastable particle. The equation for the current in the gap is now modified to

$$I = I_0 \frac{e^{\alpha d}}{1 - \gamma[e^{\alpha d} - 1]} \qquad (4.2)$$

4.8 Townsend's Criterion for Breakdown

If the denominator in Equation 1.2 tends to zero, the current will tend to increase to the point where its value is only controlled by the external components of the supply circuit. The criterion for breakdown is therefore given as or

$$1 - \gamma[e^{\alpha d} - 1] = 0 \qquad (4.3)$$

Since $e^{\alpha d} \gg 1$, the breakdown criterion is met if $\gamma e^{\alpha d} \approx 1$ and breakdown will occur if $\gamma e^{\alpha d} > 1$.

4.9 The Radiative Attachment Process

In some cases where an electron collides with an atom of an electronegative gas, such as oxygen or water-vapour in air, the collision becomes an attaching collision. This often happens when electrons hit oxygen atoms in air, since they lack one electron in their outer shells. The radiative attachment collision releases electromagnetic energy such as

$$e^- + O_2 \rightarrow O_2^- + hf \qquad (4.4)$$

This energy is in the form of electromagnetic radiation. It supplies the photons that may bombard

either the cathode causing secondary electronic emission, or photo-ionise atoms to provide initiating electrons for successive avalanches. This opinion process helps to make the corona self-sustaining.

An attachment coefficient η is the average number of electron attaching collisions per unit travel. Here the expression for current is given by [32]

$$I = I_0 \left[\frac{\alpha}{\alpha - \eta} e^{(\alpha - \eta)d} - \frac{\eta}{\alpha - \eta} \right] \qquad (4.5)$$

and when primary, secondary, and attachment processes are all taken into account the current equation is then given by [33]

$$I = I_0 \frac{\dfrac{\alpha}{\alpha - \eta} e^{(\alpha - \eta)d} - \dfrac{\eta}{\alpha - \eta}}{1 - \left[\dfrac{\alpha\gamma}{\alpha - \eta} e^{(\alpha - \eta)d} - 1 \right]} \qquad (4.6)$$

Assuming that, $e^{(\alpha - \eta)d} \gg 1$, the denominator of this can be manipulated to yield

$$\ln(\alpha - \eta) - \ln \alpha \eta = (\alpha - \eta)d \qquad (4.7)$$

which can only be defined if $\alpha \geq \eta$. This is used to determine the criterion for the creation of corona discharge. Breakdown can occur if $(\alpha - \eta) > 0$.

4.10   The Effect of Non-uniform Fields

Townsend's criterion, as given above, is sufficient to explain breakdown between parallel plates where the number of attaching collisions in the gas is insignificant. Where the field is non-uniform, the onset criterion for negative corona [34] may be written as

$$1 - \gamma e^{\int_{b}^{r_c} (\alpha - \eta)dx} = 0 \qquad (4.8)$$

where photo-ionisation is the main secondary ionising coefficient and where the integration is from the conductor surface to the limit of ionisation. The field is also nonuniform in the concentric cylinder configuration (Figure 4.4) with the highest stress being around the centre electrode. When applied to a concentric cylinder, the negative onset criterion may be expressed as follows:

$$1 - \gamma e^{\int_{r_c}^{r_0} (\alpha - \eta) dr} = 0 \tag{4.9}$$

The streamer criterion can be used to predict the onset of positive corona and is written, [35]:

$$\int_0^{x_c} (\alpha - \eta)\, dx \approx 18 \tag{4.10}$$

$$\text{or} \quad \int_{r_c}^{r_0} (\alpha - \eta)\, dr \approx 18 \tag{4.11}$$

for the concentric cylinder configuration.

In the concentric cylinder configuration, the corona is confined to those areas in the field where $(\alpha - \eta) > 0$. The equations given to calculate the current are complicated by the fact that the ionising and attachment coefficients are affected by the electric stress, ambient temperature and air pressure.

The gap between the cylinders may be seen as two regions. The inner region where ionisation processes dominate ($\alpha > \eta$), and the outer region where the electric field is stress is too weak to maintain ionisation ($\alpha < \eta$). The ionisation limit is defined as the boundary where $\alpha - \eta = 0$. The values of α and η depend primarily on the electric field strength G. The following relations are used to calculate the ionising and attachment coefficients [36]:

$$\alpha = \delta \cdot 3632 e^{-168.0 \frac{\delta}{G}} \dots \left(1.9 < \frac{G}{\delta} < 45.6 \right)$$

$$= \delta \cdot 7385 e^{-200.8 \frac{\delta}{G}} \dots \left(45.6 < \frac{G}{\delta} < 182.4 \right) \qquad (4.12)$$

and
$$\eta = \delta \left[9.9865 - 0.541 \cdot 10^{-3} \left(\frac{G}{\delta} \right) + 1.118 \cdot 10^{-8} \left(\frac{G}{\delta} \right)^2 \right] \qquad (4.13)$$

where
$$\delta = \frac{p}{101.3 \cdot 10^3} \cdot \frac{293}{273 + \theta} \qquad (4.14)$$

Where p is the air pressure in kPa and θ is the air temperature in °C. The units for the electric stress G are kVcm^{-1}. The air density factor δ defines the effect of air pressure and temperature on the ionising and attachment coefficients. These values of α, η, and δ will be used to predict the onset of corona.

4.11   Effect of Space Charge

Air contains oxygen that contributes to it being an electronegative gas. Positive ions are formed when atoms lose electrons due to collision. Some of these freed electrons attach themselves to air molecules to create negative ions. These ions, being much heavier, have a much lower mobility than the electrons. They tend to accumulate in the space between the concentric cylinders to form quasi-stationery ion clouds or 'space charges', which cause local distortions in the electric field. This affects the development of corona discharges.

4.12   Corona Onset

The onset of corona on a conductor surface depends primarily on the surface electric field stress

G_c and the air density δ. G_c in turn is determined by the applied voltage V between the electrodes, the conductor radius r_c, the conductor surface condition, and the existence of space charge. If V increases until the value G_c on the wire surface just exceeds the breakdown strength of air, the air becomes ionised and forms a conductive layer of corona around the conductor surface that effectively increases the radius of the conductor [37]. If this radius increase causes G_c to reduce then the corona will remain, otherwise spark-over will occur.

The exact value of G_c at which corona onset occurs is difficult to determine because, in addition to vagaries of the variables concerned, there does not appear to be consistency in the references surveyed. This is supported by Loeb who comments on some authors who defined the threshold of corona onset being the appearance of measurable current, while others defined it in terms of the appearance of visible glows or other such manifestations [38].

Peek defines a critical visual corona point that is the point at which a hissing is first heard, when a pale violet light is seen around the conductors [39]. Sarma and Janischewskyj define the onset of corona as the initiation of a self-sustaining discharge near the conductor surface that occurs when the conductor surface voltage gradient reaches a critical value [40] and this is repeated by Maruvada [41]. Most equations used to determine the onset of corona are used to estimate the onset of visual corona. This however does not take into account corona phenomena that occur at slightly lower voltages, which cannot be heard or seen without specialised equipment.

Loeb defines the corona threshold as occurring when there is a sudden jump in the current just before the initial appearance of the corona, (as seen at point *b* in Figure 4.1). The thresholds can then be further divided into burst pulse threshold, streamer threshold, Trichel pulse threshold, or glow discharge threshold each of which can occur under different polarities or other conditions.

Phillips quotes an ANSI standard that defines the corona voltage at which the corona just disappears as the applied voltage is being reduced [42]. This is the threshold of corona extinction.

For laboratory tests the threshold values at which corona is first seen with increasing voltage, onset value, and at which corona is last seen with decreasing voltage, offset value, are described by Phillips, Olsen, and Pedrow [43]. The use of this is reported later in this document.

Corona onset can also be defined in terms of Townsend's breakdown criteria so that it can be determined mathematically using Equations (4.8-4.14).

Chapter 5 Determining Corona Onset in a Corona Cage

The use of the corona cage for corona studies is well established for corona studies around high voltage AC conductors [44]. Its use for HVDC conductors is limited by difficulties in predicting the effect of space charge surrounding the conductor on the surface stress [45]. To evaluate this, an aluminium conductor of diameter 1.76 cm was placed in the corona cage in the HVDC laboratory at the UKZN. This is the same diameter as that of the shield wire and the results of observations were compared with observations using the actual shield wire. The corona cage and aluminium conductor comprise a concentric cylinder configuration. The voltage to cause the onset of corona for negative polarities was predicted using relevant literature and then compared with the results of laboratory tests.

Theoretical determination of the onset voltage was done in two steps. In the first step, the electric field strength on the surface of the conductor that would just cause corona to start was determined. The second step was to determine the voltage that needed to be applied to induce the required stress.

Calculated onset voltages for the smooth aluminium conductors are used to estimate the onset voltage for a stranded conductor.

5.1   Calculation Methods to Determine the Onset Stress

Several methods have been sited in literature. The following methods are used to compare estimates of the onset voltage, (approximate dates of publication are given in brackets):

5.1.1 Peek's Formula (1929), [46]

Peek is credited with the first formula to estimate the onset corona and so the basis for his
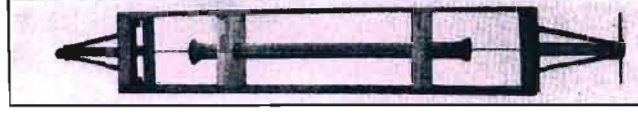
Figure 5.1   Concentric Cylinder Apparatus   (*Peek*)

reasoning is presented in some detail. It is used to estimate the gradient on the surface of a smooth

polished wire placed in the centre of a cylinder as shown in Figure 5.1. Its cross is that of a

concentric cylinder configuration section as depicted in Figure 4.3 and repeated here in

Figure 5.2, where the inner conductor has a radius of r_c, and the outer cylinder R. When visual

corona starts, it will have a radius of r_0. Peek called the distance between r_c and r_0 the energy

distance. At the onset of corona, the gradient on the conductor surface is given by

$$G_c = \frac{V}{r_c \ln \dfrac{R}{r_c}} \tag{5.1}$$

The gradient at the border of ionisation a cm away from the surface is

$$G_O = \frac{V}{r_0 \ln \dfrac{R}{r_c}}$$

$$= \frac{V}{(r_c + a)\ln \dfrac{R}{r_c}} \tag{5.2}$$

Peek has empirically shown that a is a function of r_c, $a = f(r_c)$:

$$G_O = \frac{V}{(r_c + f(r_c))\ln \dfrac{R}{r_c}} \tag{5.3}$$

Figure 5.2   Concentric Cylinder Configuration
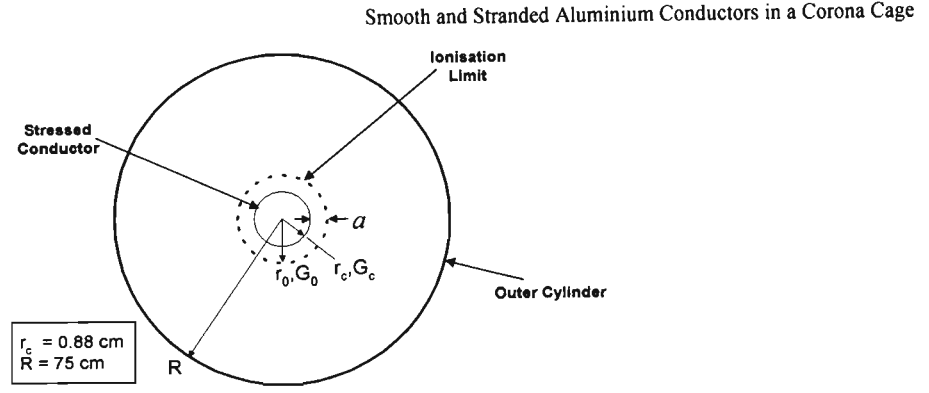
By dividing the Equations (5.1) and (5.3), he has shown that $\dfrac{f(r_c)}{r_c} = \dfrac{\alpha}{\sqrt{r_c}}$ so that

$$G_c = G_0 \left(1 + \frac{\alpha}{\sqrt{r_c}} \right) \qquad (5.4)$$

Inclusion of the air density factor δ, and the wire stranding (irregularity) factor m gave the following for the concentric cylinder configuration:

$$G_c = 31\, m\, \delta \left(1 + \frac{0.308}{\sqrt{\delta\, r_c}} \right) \quad [\text{kVcm}^{-1}] \qquad (5.5)$$

This is the classic 'Peek's formula for concentric cylinders', (for parallel wires $G_0 = 29.8$ kV/cm and $\alpha = 0.301$).

5.1.2 Observations on Peek's Formula

Several researchers have claimed that Peek concentrated on conductors of very small diameter, eg, [47]. However, he claims to have good results for parallel conductors with diameters of up to 8.9 cm [48]. In addition he provided data for DC and AC corona and spark-over voltages for concentric cylinders with the inner conductor radii from 0.0038 cm to 1.110 cm. The radius of the outer cylinder diameter is fixed at 3.81 cm while different diameters of wire are used in the centre. So the field enhancement factor (which is the ratio of gap peak stress to average stress)

varies widely from 145 for the smallest radius tested to 2 for the largest. This means that the field is highly non-uniform for the smallest centre conductor radii and approximately uniform for the largest. The fact that the corona and spark-over voltages are almost equal for the largest radii tested confirms that the simulation becomes closer to a parallel plate simulation.

Evidently Peek did not appreciate the effect of field inhomogeniety close to the highly stressed electrode on the corona onset. The field inhomogeniety (or field divergency) factor d_f is given by

$$d_f = \left[-\frac{dG_c}{dr} \cdot \frac{1}{G_c} \right]_{r=r_c} \tag{5.6}$$

Which can be used to calculate the minimum field required for corona onset for rod/plane gaps [49].

Differences between Peek's calculations and modern results may be more due to limitations of equipment and instrumentation available at the time and the fact that the effects of photo-ionisation of air by photons of a corona discharge were unknown before 1934 [50]. This could have lead to pseudo-coronas due to the reflection of light on the inner surface of the outer cylinder. He used outer cylinders of relatively small diameter so that as larger wires were tested, so lower field enhancement factors were encountered and greater internal reflectance experienced. The confined geometry of the concentric cylinders also would have conserved the products of any chemical reactions due to the corona [51], as can be seen in Figure 5.1 and particularly in the apparatus used for evaluating the effect of air pressure as shown in Figure 5.3.

It is however somewhat of a tribute to him that, while other similar formulae have been proposed, his is still the one of preference, and the results it gives are acceptable for many applications. He
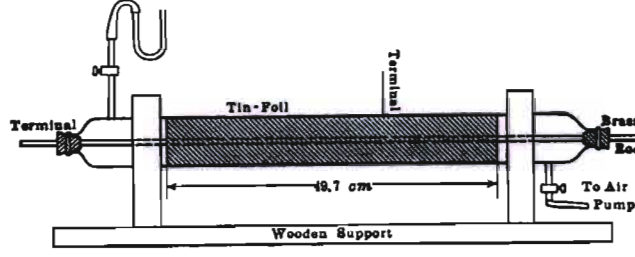
Figure 5.3   Apparatus for Determining the Effect of Pressure
on the Strength of Air   (*Peek*)

notes a difference of up to 6% between positive and negative corona onset voltages, but does not

give details and it is therefore difficult to draw conclusions regarding these claims.

5.1.3   Whitehead's Formula (1929), [52]

Sarma and Janischewskyj quote formulae (5.7) and (5.8), which have been derived by Whitehead,

which may be used to estimate the onset stress for positive and negative corona, (they do not

provide any further information).

Positive corona onset, $G_{c+} = 33.7\delta + 8.13\sqrt{\dfrac{\delta}{r}}$ [kV/cm]   (5.7)

Negative corona onset, $G_{c-} = 31.02\delta + 9.54\sqrt{\dfrac{\delta}{r}}$ [kV/cm]   (5.8)

5.1.4   Heymann's Formula (1965), [53]

Heymann is the first to take into account the effect of attachment, and has analysed the problem

based on the approximate Schumann criterion. He pointed out that there will always be a region

where attachment is greater than ionisation in a non-uniform field that has corona. He claimed

that no previous work had allowed for that and went on to show that the value of attachment has

important consequences in establishing the corona onset voltage. His work also shows that the

radius of the limit of corona occurs approximately where attachment is equal to ionisation. (This criterion is still used to this day.)

He claimed that the calculated onset electric stress values for larger diameters of wire were too high when Peek's formula was used. He has proposed equation (5.9.)

$$G_c = 24 \pm 3.3 + \frac{2.25}{\sqrt[0.4]{(r_c \delta)}} \quad [kV/cm] \tag{5.9}$$

Heymann also lists the findings of seven other investigators who developed formulae of a similar type.

It is interesting that in response to Heymann's proposal, Einhorn suggested that it was more practical to fit Heymann's data with equation (5.10).

$$G_c = 27.3 \delta \left(1 + \frac{0.0388}{\sqrt{\delta\, r_c}} \right) \quad [kVcm^{-1}] \tag{5.10}$$

because the square root is so '... convenient for slide-rule work' [54]. This perhaps identifies the real motivation of Peek's empirical formula, which has been followed by others. This kind of motivation no longer applies to the modern day with the availability calculators and computers. Some of the following methods require extensive calculations that are best done with a programable calculator, or preferably, a computer.

5.1.5 Steady State Analysis of the Ionisation Layer (1969), [55]

Sarma and Janischewskyj have presented a theoretical analysis of the electric-field distribution in the ionisation layer around a DC conductor that is under corona discharge for both polarities. They have analysed the condition of onset based on Townsend theory by taking the primary

ionisation coefficient α and the secondary coefficients for photo-ionisation, γ_p, and positive ion

impact γ_i into account as a follow on to Heymann's work. In addition they consider the absorption

of photons and the geometric factors thereof.

For the case of the negative conductor both photo-ionisation, and positive ion impact contribute

to the corona, whereas for the positive conductor, only photo-ionisation occurs. This substantiates

observations of corona onset usually occurring at a lower stress for negative polarities.

The calculations required are extensive and beyond the scope of this dissertation, however Sarma

and Janischewskyj provided graphs showing their results and readings were taken from these as

required.

5.1.6 Abdel-Salam and Khalifa's Formula (1974), [56]

Khalifa has established by experiment and computation that corona discharges start at different

surface field stress depending on the polarity of the applied voltage [57]. For air density values

within the range $(0.9 \leq \delta \leq 1.1)$, Khalifa has shown that equation (5.11) can be used to

determine the critical value of surface field stress.

$$G_{c\pm} = A_\pm \delta + B_\pm \sqrt{\frac{\delta}{r_c}} \quad [\text{kVcm}^{-1}] \qquad (5.11)$$

Values for A and B have been determined by Khalifa. These have been used to calculate the

critical onset stress $G_{c\pm}$. These values are given in Table 5.1.

Table: 5.1 Values of Constants *A*, *B* *(Khalifa)*

Conductor	A [kVcm^{-1}]	B [kVcm^{-1}]
Positive	$31 \leq A_+ \leq 39.8$	$11.8 \leq B_+ \leq 8.4$
Negative	$29.4 \leq A_- \leq 40.3$	$9.9 \leq B_- \leq 7.3$

5.1.7 Zaengl and Nyffenegger's Formula (1974), [58]

Zaengl and Nyffenegger have studied Peek's formula in detail and have found that for values of $(\delta r_c) > 1$ cm it gives higher values than were experimentally observed. They have developed the analytical expression (5.12).

$$\left(\frac{G_c}{\delta}\right)^2 - 2\left(\frac{G_c}{\delta}\right)G_0 \ln\left[\frac{1}{G_0}\left(\frac{G_c}{\delta}\right)\right] - G_0^{\,2} = \frac{42}{\delta r_c} \tag{5.12}$$

This equation holds as long as the surface field stress of the inner cylinder is greater than that of the outer cylinder. It must be solved iteratively.

5.1.8 Washington State University Optimisation Criterion (1996), [59]

All the preceding formulae apply strictly to concentric cylinder geometry, and in some cases may be crudely modified using a wire stranding factor, which can only be obtained from experimental observations. These formulae are not appropriate for other geometry. In contrast, a criterion has been developed at the Washington State University (WSU) which is extremely useful in that it may be applied to any geometry.

As may be seen by the formulae proposed by Whitehead, corona starts at a lower conductor surface stress value when the highly stressed electrode is negative. This is confirmed with calculations by Sarma and Janischewskyj, [60] but show that the negative onset corona value is only about 4% less than that of a positive one for a conductor of 2 cm radius or greater. The difference is less for smaller conductors.

Assume (for a negative conductor) that N_c free electrons are created on its surface at the position where $r = r_c$. The number of free electrons N_0 at position $r = r_0$ can be calculated using

$$N_0 = N_c e^{\int_{r_c}^{r_o}(\alpha - \eta)dr} \tag{5.13}$$

Where α, the ionisation coefficient, and η, the attachment coefficient, are functions of the electric stress and the air density as described in Equations (5.10 – 12). The number of initial electrons is unknown and so the following ratio is used

$$N^* = \frac{N_0}{N_c} = e^{\int_{r_c}^{r_o}(\alpha - \eta)dr} \tag{5.14}$$

Pedrow has shown that the critical value that transforms the avalanche into a self propagating streamer is given by $N^* = 3500$ that corresponds with a secondary ionising coefficient of $\gamma = 2.86 \cdot 10^{-4}$ when using Equation (5.8). This gives results that closely agree with Zaengl and Nyffenegger's formula.

Phillips, Olsen, and Pedrow have successfully used corona onset surface optimisation software to design electrode surface shapes (not stranded conductors) so that they can have the highest possible onset voltage, [61].

5.2   Influence of Space Charge on Corona Onset

The electric field is the sum of the applied (Laplacian) field and the field due to the positive space charges (positive ions created by ionisation), or negative space charges (negative ions created by attachment). The ionisation region is least disturbed by its own space charge as the charged particle velocities are high and the electric stress is high. It has been found sufficient to assume a field distribution across the ionisation region as calculated from the geometry and the applied voltage, as well as the gross effects of the space charges in the drift region. This approximation breaks down if the number of electrons in an avalanche exceeds 10^6 to 10^8, [62].

If the conductor is positive, any free electrons in the area between r_0 and R are rapidly removed by attachment as in this region the attachment coefficient is greater than ionisation coefficient. The corona discharge can only occur if secondary electrons are created in the region between r_c and r_0 where the ionisation process dominates. The only secondary process that is operative is that of gaseous photo-ionisation which takes place close to the positive conductor to provide secondary electrons to sustain the discharge.

With the negative conductor, ionisation causes liberated electrons to move outwards toward the ionisation limit at r_0. Their mobility is much higher than the positive ions they leave behind which move toward the negative conductor at a relatively slower pace. The electrons become attached outside the ionisation limit forming negative ions and liberating photons which feedback to cause further photo-ionisation. The positive/ negative ion space charges set up a field that is opposite in polarity to the Laplacian one and tends to cancel with it causing the current to be shut off. With the cessation of current, the positive ions are taken up by the negative conductor, and the negative

ions are swept away in the direction of the outer cage. The process starts from scratch again to

form a new 'Trichel Pulse'.

5.3   Effect of Polarity on Corona Onset

From the description of the different processes for positive and negative corona, it is seen that

positive corona is primarily due to photo-ionisation, while both photo-ionisation and ionisation

by impact occur with the negative conductor. This is the case for normal atmospheric

temperatures and pressures, and so it seems that the onset voltage for the negative conductor is

lower than that for the positive conductor. This is supported by most sources, but both

Cobine [63], and Khalifa [64] assert a minority view that the onset of positive corona is at a

slightly lower stress than the negative case. Since the effect of polarity on corona onset has been

reported for different conductor configurations, at various temperatures and pressures, in different

types of gases, getting consistency is difficult. It was therefore deemed necessary to observe the

onset of corona for a sample of the aluminium stranded conductor, under normal atmospheric

temperature and pressure conditions. This was done and the results are reported in Chapter 11.1.

Following the onset of corona, the change in conductor surface gradient due to increase of

current, has been found by Sarma and Janischewskyj to be negligible for currents less than

1 μA/cm of conductor length as is normal for DC transmission lines used in practice [65].

5.4   Calculation of Onset Voltage for the Smooth Aluminium Rod Conductor

It is necessary to predict the onset of corona on a known conductor placed in the centre of a

corona cage to compare the observations with theory. For this purpose the corona cage at the DC

high voltage laboratory at the UKZN was used. The cage is 1 m long with two 0.5 m guard rings, it has a diameter of 1.5 m and is suitable for a single conductor with a diameter of 1 cm to 4.5 cm [66]. A polished aluminium conductor with an outer diameter of 1.76 cm is placed at the centre of it.

The methods of estimating the onset stress values have been detailed in Chapter 5 and were used to calculate the onset stress. For convenience a computer program using Matlab®, [67] has been written to calculate the estimated values of the expected onset conductor surface stress as well as the expected onset voltage for each of the above equations. The program listing is given in Appendix F.

The onset values using the Peek, Whitehead, Heymann, and Khalifa methods were simply calculated using the given formulae.

For Sarma and Janischewskyj, readings were taken from simple graphs provided by them.

The formula given by Zaengl and Nyffenegger is solved by using a simple iterative routine. The result from the Peek calculation is increased by ten percent to start with a value known to be high. The onset stress value is then repeatedly estimated with progressively smaller estimates of surface stress until the equation is solved to the nearest 1E-4.

The WSU corona onset criterion had to be determined in three steps, making the use of a computer essential. First the onset stress was determined by determining the value of stress G_0 that occurs at the point where the attachment coefficient α is equal to the attachment coefficient η. This was done using a simple iterative process by first using Peek's value to calculate a value

known to be high and then repeatedly reducing it to a value of G_0 that resulted in $(\alpha - \eta) \leq |1\text{E-4}|$. This value of G_0 was used to calculate the corona radius limit r_0 for an applied voltage V that had also been estimated using an exaggerated version of Peek's value. The integral $\exp\left(\int_{r_c}^{r_0} (\alpha - \eta) dr\right)$ was performed and compared with 3500. When found to be too high, the value of V was reduced, and the integration performed again until agreement to within 1E-4 was obtained. The curve of $(\alpha - \eta) = f(r)$ has an increasingly negative slope, (similar to exponential decay). Integration by the midpoint method continually gives underestimates of the true values, while a trapezoidal method consistently gives slightly high values. A quadratic

Table: 5.2   Expected Corona Onset Stress for Conductors (STP)
$R = 75$ cm, $r_c = 0.88$ cm

Method	Conductor Onset Stress [kVcm⁻¹]	Applied Onset Voltage [kV]	
		Aluminium Rod	Shield Wire $m = 0.73$
Peek	41.18	161.10	117.60
Whitehead (+ve)	42.37	165.70	120.96
Whitehead (-ve)	41.19	161.10	117.60
Heymann (min)	35.65	139.40	101.76
Heymann (max)	42.25	165.30	120.67
Sarma and Janischewskyj (+ve)	42.50		
Sarma and Janischewskyj (-ve)	40.60	158.80	115.92
Khalifa (+ve, min)	43.58		
Khalifa (+ve, max)	48.75		
Khalifa (-ve, min)	39.95	156.30	114.10
Khalifa (-ve, max)	48.08	188.10	137.31
Zaengl & Nyffenegger	41.01	160.40	117.09
WSU Onset Criterion	41.91	163.90	119.65
Average for Negative Onset	41.42	162.01	118.27

solution of the integration using Simpson's Rule provides sufficient accuracy, [68].

Matlab® calculated all these values, and the results are summarised in the second column of Table 5.2.

The applied voltage at which the onset of corona will occur (the onset voltage) was next calculated knowing the relationship between the applied voltage and the conductor surface stress. The conductor surface roughness and its state needed taken into account, as well as the atmospheric conditions. Neglecting the effect of space charge, the relationship between the applied voltage and the surface stress is given by equation (4.1) and is repeated here:

$$G_C = \frac{V}{r_C \ln \dfrac{R}{r_C}} \quad [\text{kVcm}^{-1}] \tag{5.15}$$

This relationship may be rearranged to make V the subject of the equation and substituting $r_c = 0.88$ cm, and $R = 75$ cm to give

$$V = G_c r_c \ln \frac{R}{r_c}$$
$$= 3.91 \cdot G_c \tag{5.16}$$

This has been used to calculate the expected applied voltages for the smooth aluminium rod given in column three of Table 5.2. These values assume ideal conditions where the centre cylindrical conductor is smooth and highly polished. In practice the conductors in use are usually stranded and subject to weathering. The effects of these variations in conductor surface were discussed by Peterson in 1933 (see Table 5.3) and are still in use today, [69]. The text does not provide for the combining of factors for a conductor that have a surface condition that conforms to more than one item in the table. The sample of shield wire used in the corona cage have 12 outer strands. It was

Table: 5.3   Stranded Conductor Surface Factors   *(Peterson)*

Condition of Conductor	m*
New, unwashed	0.67 - 0.74
Washed with grease solvent	0.91 - 0.93
Scratch-brushed	0.885
Buffed	1.00
Dragged and dusty	0.72 - 0.75
Dragged and dusty, weathered (5months)	0.945
Weathered at low humidity	0.92
For general design	0.87 - 0.90
7-Strand concentric lay cable	0.83 - 0.87
19-, 37-, 61-Strand lay cable	0.80 - 0.85

* Determined for AC line voltages

washed with a grease solvent and has a rough surface as if it had been dragged. Using a surface factor of m = 0.73 for a dragged conductor seemed appropriate. This was used to estimate the onset voltage for the bare stranded conductor by calculating $V_{STR} = m \cdot V_C$. This was done and the results are given in column four of Table 5.2.

The average expected onset values are presented in Table 5.2. The negative onset was predicted to occur at about – 162 kV for the smooth aluminium rod and – 118 kV for a sample of stranded shield wire.

Chapter 6   Calculation of Maximum Shield Wire Surface Gradient

Where smooth surfaced conductors are used, simple methods exist which may be used to estimate the surface gradients of standard powerline configurations. Corona onset gradients may be further estimated using surface roughness or condition factors. For stranded conductors, only the average strand surface gradient can be estimated. To calculate peak surface stresses, and to plot strand surface stress variations, it is necessary to address the strands individually using field plotting methods.

The shield wire surface gradient was calculated using two methods.

- The Method of Images, based on Maxwell's equations, is used to provide estimates of the conductor surface charge to verify the results obtained from the Boundary Element Method.

- The Boundary Element Method, done using a computer software program supplied by Integrated Software called 'ELECTRO', was used to do the necessary electrostatic analyses required.

The basis of each method is explained before it is used.

6.1   Method of Images

This method is described in Khalifa [70] and has been developed as required for this application.

The conductor bundle and shield wire configuration given in Figure 6.1 was used to define the geometric layout of the HVDC line. An expression $[V] = [P] \cdot [Q]$ was developed to estimate the conductor charges from the conductor potentials and dimensions. The conductor charges were then calculated using a spreadsheet program.

For this application it was assumed that the area around the conductors is free of space charge and could be analysed using Laplace's equation, $\nabla^2 \phi = 0$, (where ϕ is the electric potential).

To simplify the calculation, the main conductor bundle was assumed to consist of four cylindrical smooth surfaced conductors each having the specified outside diameter of 31.8 mm. The shield wire was seen as twelve cylindrical conductors, each representing one conductor strand with a diameter of 3.52 mm.

Each conductor was given a potential of V_i and charge q_i per unit of length where ($i = 1,2,3,4$) for the main conductors and ($i = 5,6,7,...,16$) for the strands.

The effect of the ground plane is simulated by mirror images of the charges q_i to ensure that the potential at every point on the plane is zero.

The potential of each conductor is determined by ALL the other conductors and their images. For example, the potential of conductor 1 due solely to conductor 12 and its image (Figure 6.1) is given by (6.12).

$$V_1 = \frac{q_1}{2\pi\varepsilon} \ln\left(\frac{b_{1;12}}{a_{1;12}}\right)$$

(6.1)
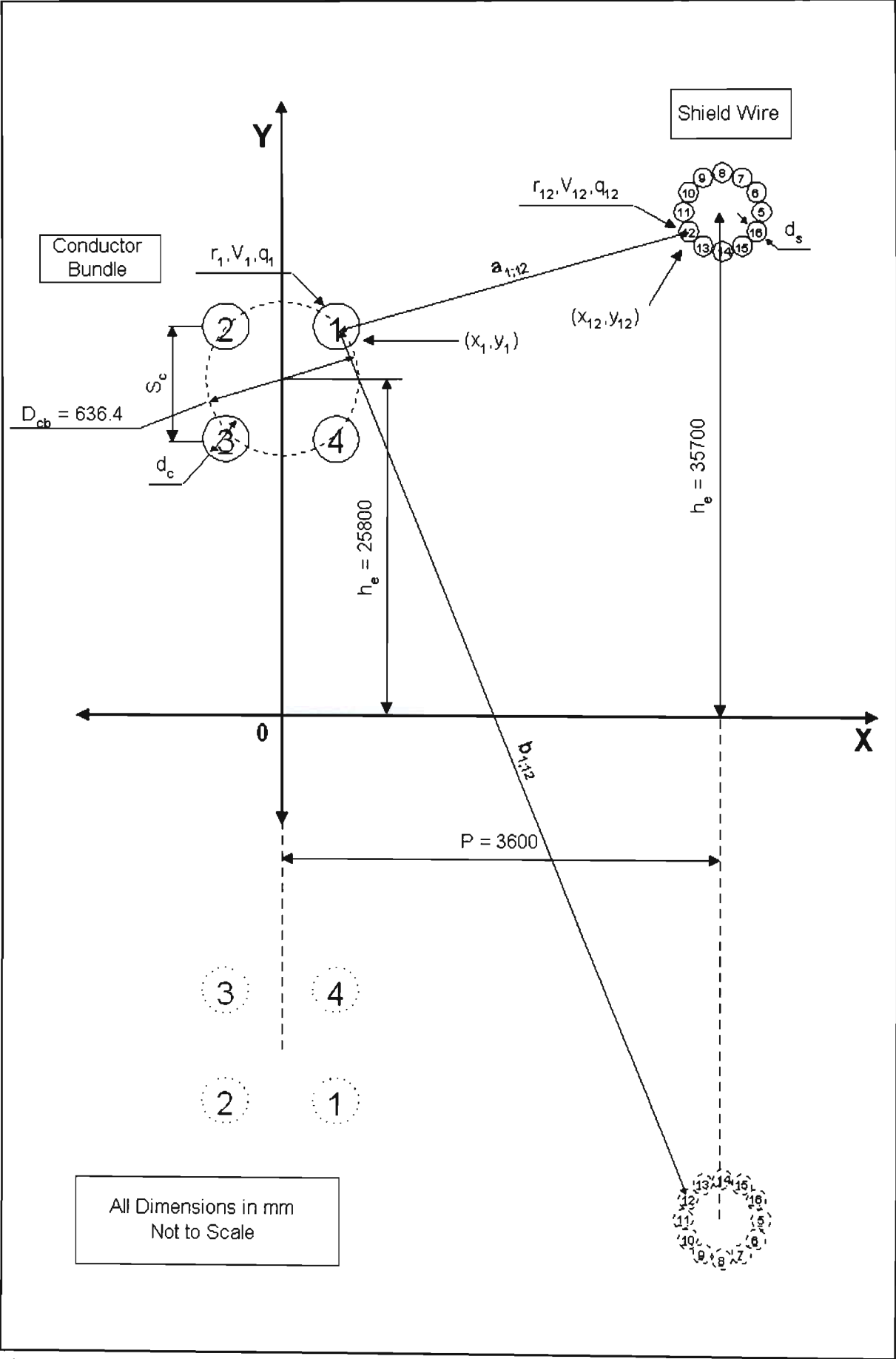
Figure 6.1   Details of Conductor Dimensions for Images Calculation

Where $a_{1;12}$ and $b_{1;12}$ are the distances shown in Figure 6.1, and ε is the absolute permittivity.

For air the relative permittivity, $\varepsilon_r = 1.000576$ Fm^{-1} at standard temperature and pressure [71], while the permittivity of free space $\varepsilon_0 = 8.854188 \cdot 10^{-12}$ Fm^{-1} [72]. So a value of $\varepsilon = \varepsilon_0 \cdot \varepsilon_r = 8.859288 \cdot 10^{-12}$ Fm^{-1} is used for the absolute permittivity.

For simplicity the charge is assumed to be concentrated at the centre of each conductor. This is based on the assumption that the conductor separations and heights are much larger than their diameters. (With the shield wire the strands are actually touching that distorts the surface charge distribution, but not the total charge, as will be shown later.)

The resultant potential of conductor 1 is the sum of the potentials due to all the other conductors is and is given by

$$V_1 = \sum_{j=1}^{16} \frac{q_j}{2\pi\varepsilon} \ln\left(\frac{b_{1;j}}{a_{1;j}}\right) \tag{6.2}$$

In general the potential of any of the conductor i is given by

$$V_i = \sum_{j=1}^{16} \frac{q_j}{2\pi\varepsilon} \ln\left(\frac{b_{i;j}}{a_{i;j}}\right)$$
$$= \sum_{j=1}^{16} q_i \cdot P_{i;j} \tag{6.3}$$

where $P_{i;j} = P_{j;i} = \dfrac{1}{2\pi\varepsilon} \ln\left(\dfrac{b_{i;j}}{a_{i;j}}\right)$ since $a_{i;j} = a_{j;i}$ and $b_{i;j} = b_{j;i}$.

This is used to set up sixteen simultaneous equations:

$$V_1 = q_1 P_{1;1} + q_2 P_{1;2} + \ldots + q_{16} P_{1;16}$$

$$V_2 = q_1 P_{2;1} + q_2 P_{2;2} + \ldots + q_{16} P_{2;16}$$

$$\vdots$$

$$V_{16} = q_1 P_{16;1} + q_2 P_{16;2} + \ldots + q_{16} P_{16;16} \tag{6.4}$$

Which can be represented in matrix form

$$\begin{bmatrix} V_1 \\ V_2 \\ \vdots \\ V_{16} \end{bmatrix} = \begin{bmatrix} P_{1;1} & P_{1;2} & \cdots & P_{1;16} \\ P_{2;1} & P_{2;2} & \cdots & P_{2;16} \\ \vdots & \vdots & \cdots & \vdots \\ P_{16;1} & P_{16;2} & \cdots & P_{16;16} \end{bmatrix} \bullet \begin{bmatrix} q_1 \\ q_2 \\ \vdots \\ q_{16} \end{bmatrix} \tag{6.5}$$

6.2   Calculation of the Values $a_{i;j}$ and $b_{i;j}$

The calculation of values $a_{i;j}$ and $b_{i;j}$ is simplified by calculating the coordinates $\left(x_i, y_j \right)$ of

each conductor on the Cartesian plane and substituting these values into the following formulae

depending on whether a *self* or a *mutual* potential coefficient is required.

Where $i = j$, self potential coefficients are calculated using [73]

$$P_{i;i} = \frac{1}{2\pi\varepsilon} \cdot \ln\left(\frac{4 y_i}{d_i} \right) \tag{6.6}$$

Where $i \neq j$, mutual potential coefficients are calculated using [74].

$$P_{i;j} = P_{j;i} = \frac{1}{2\pi\varepsilon} \cdot \ln\left(\frac{\left(x_i - x_j \right)^2 + \left(y_i + y_j \right)^2}{\left(x_i - x_j \right)^2 + \left(y_i - y_j \right)^2} \right)^{\frac{1}{2}} \tag{6.7}$$

6.3   Determining Conductor Coordinates $\left(x_i, y_j \right)$

Slightly different methods are used to determine the coordinates of the main conductors and the

coordinates of the shield wire strands.

The coordinates of the centre of the main conductor bundle are given by $(h_c, 0)$. The main conductors are numbered $(i = 1, 2, 3, 4)$. The coordinates of each conductor can then be calculated using

$$(x_i, y_i) = \left(\frac{S_c}{\sqrt{2}} \cos\left((2i-1) \cdot \frac{\pi}{4} \right), h_c + \frac{S_c}{\sqrt{2}} \sin\left((2i-1) \cdot \frac{\pi}{4} \right) \right) \qquad (6.8)$$

where S_c is the spacing between the main conductor centres in the main conductor bundle.

The coordinates of the centre of the shield wire are (P, h_e). The shield wire strands are numbered ($i = 5, 6, 7, ..., 16$). The coordinates of each strand can then be calculated using

$$(x_i, y_i) = \left(P + 0.5 \cdot d_s \cos\left((2(i-5)-1) \cdot \frac{\pi}{6} \right), h_e + 0.5 \cdot d_s \sin\left((2(i-5)-1) \cdot \frac{\pi}{6} \right) \right) \qquad (6.9)$$

where

P is the horizontal spacing between the main bundle centre and the centre of the shield wire,

d_s is the diameter of the centres of the outer strands of the shield wire, and

h_e is the height of the centre of the shield wire.

6.4 Calculation of Conductor Charge

The main conductor bundle has four conductors and the shield wire has twelve strands so sixteen simultaneous equations are required to calculate the charge on each conductor. This has been done using a Quattro-Pro spreadsheet [75] . This calculation is large and has therefore been placed in Appendices F, (maximum conductor height), and G (minimum Conductor height), with only the results summarised here. The calculation is done for the maximum and minimum specified heights of the line. Table 6.1 shows the results for the line at its maximum height at the

Table: 6.1   HVDC Line Surface Charge at Maximum Height

Summary of Results	Charge
Total conductor bundle charge	5.7310e-06 C
Total shield wire charge	-1.0612e-06 C
Maximum strand charge	-8.9038e-08 C
Minimum strand charge	-8.7834e-08 C
Average strand charge	-8.8436e-08 C

towers, while Table 6.2 shows the results for minimum line height between the towers. It can be

seen that the highest conductor charges occur at the towers where the lines have their maximum

height. Consequently all further calculations of the surface charge use the maximum height

parameters.

Table: 6.2   HVDC Line Surface Charge at Minimum Height

Summary of Results	Charge
Total conductor bundle charge	6.7273e-06 C
Total shield wire charge	-7.7070e-07 C
Maximum strand charge	-6.3670e-08 C
Minimum strand charge	-6.4784e-08 C
Average strand charge	-6.4227e-08 C

Chapter 7 Boundary Element Method

The Method of Images assumes that the charge of each conductor is concentrated at its centre. This simplification reduces the required number of simultaneous equations, and is useful for
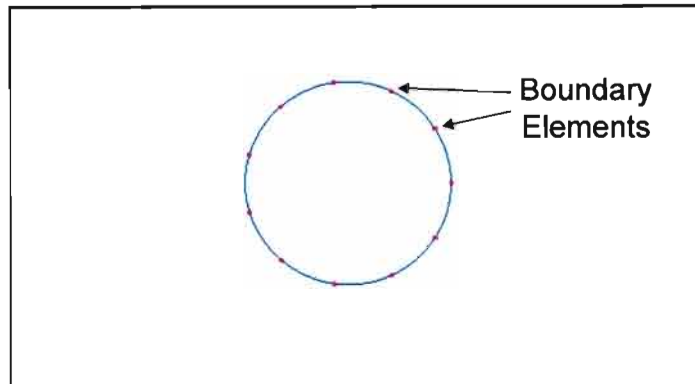
Figure 7.1   Example of BEM Element Placement

estimates. It was used to estimate the electrical charge on the conductors and will be compared with the results of the boundary element method, (BEM) simulation. The BEM does not require such simplifications and instead places boundary elements directly on the boundaries of defined geometry [76], as illustrated in Figure 7.1. This makes the BEM suitable because the electrical stress on the shield wire surface is of particular interest in this application.

BEM has the further advantage that it "... provides continuous equipotential contours that are free from discontinuities ...", and it "... provides an error check method that is inherent to the calculation of the potential function", [77].

A formal discussion on the derivation of the BEM is outside the scope of this exercise, and further information may be obtained from [78] and [79]. Instead ELECTRO, a custom software package [80], has been used to do the analysis of the electric field around the shield wire.

With this method, it is no longer necessary to simplify the calculation by representing the main conductor bundle with four cylindrical smooth surfaced conductors as was done in the Method of Images. Instead the four conductors are now represented by their outer strands as was done for the shield wire. The shield wire is represented by its outer strands, as before.

The value of absolute permittivity at STP is set at $\varepsilon = \varepsilon_0 \cdot \varepsilon_r = 8.859288 \cdot 10^{-12} \ Fm^{-1}$.

7.1   Using ELECTRO to Perform a Simulation

To perform a simulation

- a *geometric model* of the physical system is constructed using the built in geometric solver,

- *physical properties* (such as boundary conditions, boundary potentials, and exact position of boundary elements) are assigned, and

- the model is *discretized* and the solution is calculated using the *field solver*, [81].

7.2   Construction of the Geometric Model and Boundary Element Placement

A geometric model of the line to simulate the conductor dimensions was created by first defining a work space of 20 m wide and 40 m high. Line geometry was simulated with the conductor bundle and shield wire placed 1.8 m on either side of the centre, and placed at heights of 25.8 m and 36.7 m respectively. This put the coordinates of the centre of the conductor bundle at (-1 800; 25 800) and the centre of the shield wire at (1 800; 36 700). (Length units default was set to millimetres in Electro.)

The coordinates of the shield wire and conductor bundle at their highest position at the towers were used where the surface stresses are likely to be highest. These dimensions and other important details, are shown in Figure 7.5.

The representation of the main conductor cross section is shown in Figure 7.2. for which the number of boundary elements was set by ELECTRO to between 10 and 24 elements per strand. Element distribution is sufficient for the purpose. The shield wire detail is shown in Figure 7.3 with 50 boundary elements on the bottom strand and 16 per strand for the rest. The detail of the elements on the bottom strand is illustrated in Figure 7.4. More elements are placed where the
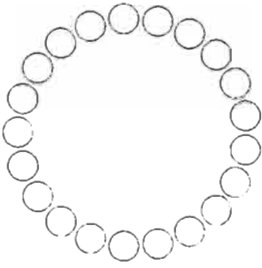
Figure 7.2
Conductor Detail
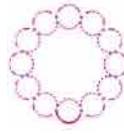
Figure 7.3
Shield Wire Detail

Figure 7.4
Bottom Strand Detail

strand will be in contact with the ADLash to reduce error.

7.3   Defining the Physical Properties

The following physical properties were set:

•   The main conductor strand boundaries are set to −533 kV, while the shield wire strand boundaries are set to 0 V.

•   The relative permittivity of the background, $\varepsilon = 1.00576\,\mathrm{Fm^{-1}}$.

•   The X-axis is chosen as a symmetric boundary, so that the geometry above the X-axis is

automatically mirrored below it as was done in the Method of Images. This ensures that

the X-axis is simulated as an infinite ground plane.
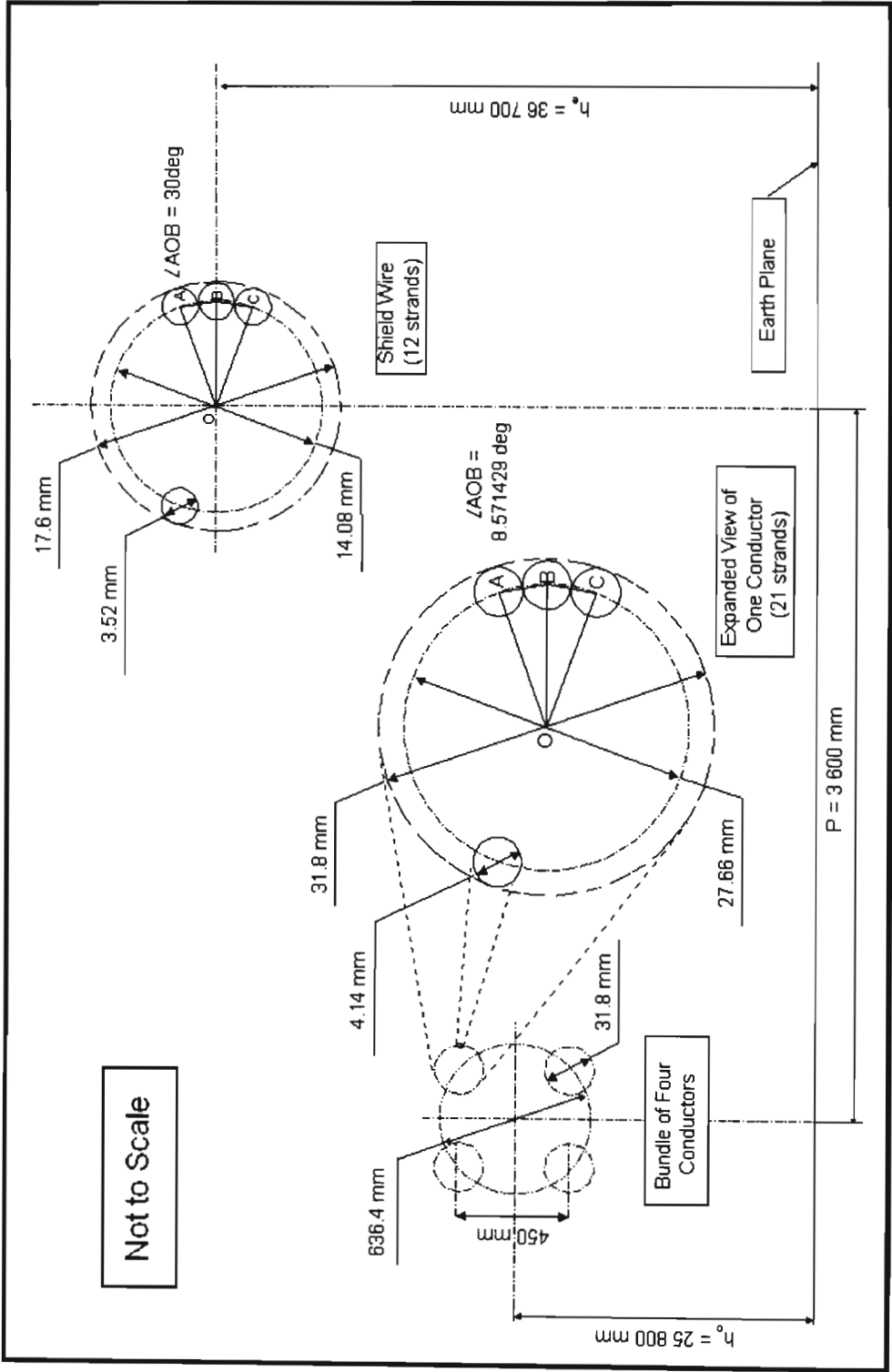
Figure 7.5   Details of Conductor Dimensions Used in the Boundary Element Method

-51-

7.4   Model Discretization and Solution

When the problem is solved, the model discretization is automatic. The automatic matrix solver was chosen, and set to *manual* (not *self adaptive*). The accuracy was set to level 1 and the nonlinear convergence factor set to 0.01, which established the exit criteria of the numerical solution.

Item	Total Charge	
Shield Wire	-1.0788e-06	C
Conductor Bundle	5.6715e-05	C

Table 7.1 Conductor Surface Charge

The model was solved and the surface charge values of the shield wire and conductor bundle were queried. The results are summarised in Table 7.1 showing values slightly higher than those for the Method of Images but not significantly so. Moyo [82] calculated an average surface stress on the conductor bundle as 19.43 kVcm^{-1} and 21.73 kVcm^{-1} on the shield wire. These were used to estimate the line charges using [83]

$$G_{ave} = \frac{q}{\pi n d \varepsilon} \tag{7.1}$$

This yielded an average shield wire charge of $q_s = 0.9518$ μC, and similarly the average charge per conductor of $q_c = 7.58686$ μC .

These values are summarised in Table 6.2 for comparison. It can be seen that all the methods agree fairly well for the shield wire given the assumptions made in each case. The method used by Moyo calculated a higher surface charge for the main conductors and this is probably due to the use of a single bundle diameter to represent the four main conductors.

Neither the method used by Moyo, nor the Method of Images gives much information regarding the distribution of charge on the conductors. Both methods assume a uniform distribution of charge over the surface of each conductor. The shield wire has almost no charge inside the strands so it

Table: 7.2   Comparing Strand Surface Charge Values

Shield Wire Strand No.	Strand Surface Charge [C]	
	Images Method	BEM Method
5	-8.82e-08	-8.97e-08
6	-8.80e-08	-8.94e-08
7	-8.78e-08	-8.93e-08
8	-8.79e-08	-8.93e-08
9	-8.81e-08	-8.95e-08
10	-8.83e-08	-8.98e-06
11	-8.87e-08	-9.01e-08
12	-8.89e-08	-9.04e-08
13	-8.90e-08	-9.05e-08
14	-8.90e-08	-9.05e-08
15	-8.88e-08	-9.02e-08
16	-8.85e-08	-9.00e-08

must be assumed that the charge is concentrated on the outside. The Method of Images does however give estimates for the surface charge of the individual shield wire strands. This is shown in Table 7.2 together with results reported by BEM for comparison. Clearly these results are very close. For all further analyses only the BEM was used because it can determine the charge distribution on the strand surfaces and hence the surface stress distribution.

Chapter 8   Shield Wire Surface Stress With and Without ADLash

The dimensions and layout of the HVDC line were simulated using the Boundary Element software package (BEM). The BEM calculations of the field stresses around the shield wire of the HVDC
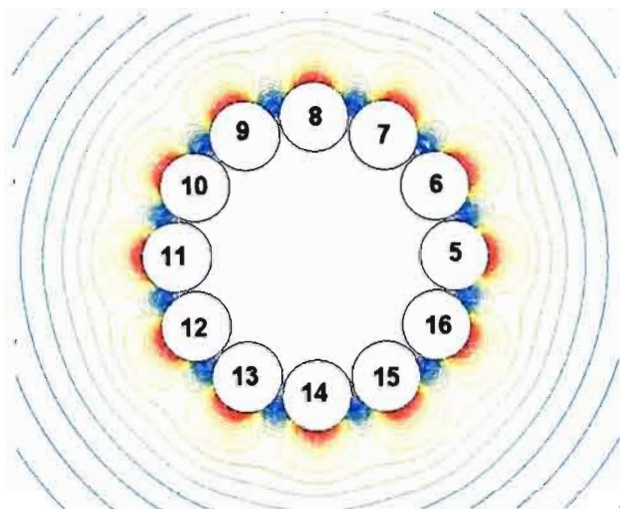
Figure 8.1   Electric Stress Around the Shield Wire

line simulation are now presented. Calculations of the field with and without the ADLash optic fibre cable are presented for comparative purposes.

8.1   Shield Wire Field

Electrostatic field contours around the shield wire are drawn as shown in Figure 8.1. This clearly shows that the highest stress is on the outer edges of the shield wire. The magnitude of the surface stress around the surface of the bottom strand is plotted in Figure 8.5.

An estimated value of corona onset was obtained from Table 5.2 where the expected onset value of a smooth cylindrical conductor was estimated to be $G_c = 41.42 \, \text{kVcm}^{-1}$ at STP. Although Peek

gives slightly different corona onset formulae depending on conductor configurations, the differences are insignificant for this application [84]. The onset stress for the shield wire may be estimated using a suitable surface factor m from Table 5.3 together with the relative air density factor δ.

As seen in the table, the value of m can vary widely, but a value of $m = 0.85$ is used.

The dependance of air density on altitude α and ambient temperature t was estimated using the following relation [85]:

$$\delta = e^{-\alpha \cdot 121 \cdot 10^{-6}} \left(\frac{293}{273 + t} \right) \tag{8.1}$$

where 180 m $< \alpha <$ 1 510 m and -5 °C $< t <$ 40 °C for the HVDC line [86] yielded a range of $0.8 < \delta < 1.1$. The onset value may be assumed to be proportional to $\delta^{\frac{2}{3}}$ [87], so the onset stress was estimated using $G_{sw} = m\delta^{\frac{2}{3}}G_c$, which resulted in a range of 29.8 kVcm^{-1} $< G_{sw} <$ 36.8 kVcm^{-1}. The peak value of the surface stress was calculated by BEM to be $G_{max} = 31.29$ kVcm^{-1}, so the probability of corona on the HVDC line is quite high. This can be clearly seen in the close up of the bottom strand of the shield wire in Figure 8.2, where only electric stress contours greater than 30 kVcm^{-1} are shown.

Figure 8.2   Bottom Strand Stress Plot of $G_{sw} >$ 30 kVcm^{-1}

8.2   Shield Wire Field with ADLash

A cross section of the ADLash optical fibre cable is now simulated in contact with the shield wire.
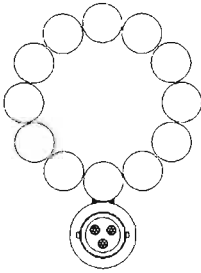
Figure 8.3   Electric Stress at the Strand/ ADLash Interface
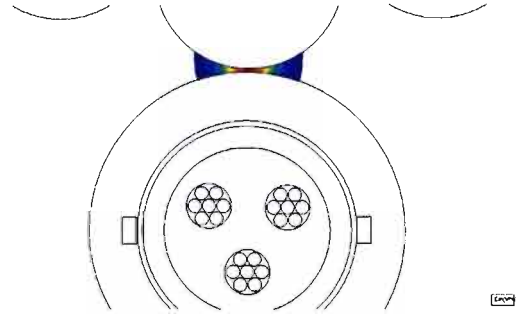
Figure 8.4   Closeup of Interface

When a dielectric with higher permittivity than air is brought in contact with air there is an enhancement of the electric field at the air/dielectric interface that follows the relation $\varepsilon_{air} \cdot G_{air} = \varepsilon_{dielectric} \cdot G_{dielectric}$ [88]. This causes the enhancement of the stress in the immediate vicinity of the interface as shown in Figure 8.3. In this figure only electric stress greater than 30 kVcm^{-1} is shown, and a closer view is shown in Figure 8.4. BEM has calculated a peak stress value of 76.6 kVcm^{-1} that is noticeably larger than the peak calculated without the ADLash.

8.3   Comparing Shield Wire Surface Stress With and Without ADLash

The magnitude of the surface stress around the bottom strand with and without the ADLash is plotted in Figure 8.5 that clearly quantifies the enhancing effect of the ADLash on the stress.

A useful measure of the effect of geometrical configurations on the electric fields surrounding

Bottom Strand Surface Stress

With and Without ADLash Attached
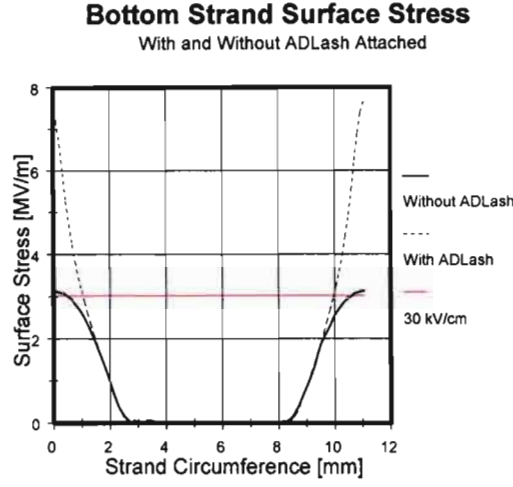
Figure 8.5 Comparing Stress with and without ADLash

conductors is the field enhancement factor defined as $f = {G_{max}}/{G_{ave}}$ [89], where $G_{max} = 31.29 \text{ kVcm}^{-1}$, and

$$
\begin{aligned}
G_{ave} &= \frac{\text{Line Voltage}}{\text{Distance between the lines}} \\
&= \frac{V_{HVDC}}{\sqrt{(h_e - h_c)^2 + (P)^2}} \\
&= \frac{533000}{\sqrt{(36.7 - 25.8)^2 + (3.6)^2}} \\
&= 0.464 \text{ kVcm}^{-1}
\end{aligned} \tag{8.2}
$$

Using values previously obtained, the enhancement factor for the case without the ADLash is given by

$$
\begin{aligned}
f_{air} &= \frac{G_{max}}{G_{ave}} \\
&= \frac{31.29 \cdot 10^3}{0.464 \cdot 10^3} \\
&= 67.4
\end{aligned} \tag{8.3}
$$

Similarly the enhancement factor for the case with the ADLash is $f_{ADL} = 165$. This suggests

that ADLash causes the maximum surface of the shield wire to be enhanced by

$f_{ADL}/f_{air} = 2.4$ times. These values are summarised in Table 8.1 that shows that, while the incidence

of corona is not an absolute certainty for the bare shield wire, it is a certainty when the ADLash

Table: 8.1 Comparing Peak Stresses and Enhancement Factors

Condition	Peak Stress [kV/cm]	Enhancement Factor f
Without ADLash	31.3	67.4
With ADLash	76.6	165

has been introduced.

Chapter 9 Simulations in the Corona Cage

Simulations of conductors with and without ADLash in the corona cage were done so that comparisons could be made with calculated values and observed tests. This simulation was done in two steps; the first being the aluminium rod (with and without ADLash) and the second being a sample of stranded shield wire (with and without ADLash). In each case the setup was simulated using the BEM software to produce an illustration of the field stress magnitude around the conductor and to draw graphs of the field stress magnitude around the surface of the relevant conductor. In each case the enhancing effect of the introduction of the ADLash was clearly seen and relevant conclusions are given.

The aluminium rod in the corona cage can be simulated as a classical concentric cylinder setup and field distribution and stresses, can easily be estimated using simple formulae. In Table 5.2 estimated that a surface stress of $G_C = 41.42$ kVcm^{-1} is required for the onset of corona that will be achieved with a negative applied voltage $V_C = -162.01$ kV. In the simulations, this voltage was applied to all configurations so that peak stresses in each case could be compared. These peak stresses were used to estimate the applied voltages that cause the onset of corona and the field enhancement factors. The effects of space charge were neglected.

In the following field distribution diagrams, field contours are only shown where the magnitude of the electric stress is greater than 30 kVcm^{-1} to illustrate where corona is likely.

9.1 Aluminium Rod With and without ADLash

Simulations with and without ADLash were done of the aluminium rod in the corona cage. The field distribution around the rod was uniformly distributed as expected and is shown in Figure 9.1. With the applied rod onset voltage of V_S = -162.01 kV, BEM calculated a peak field stress of G_{MS} = 41.42 kVcm^{-1} as expected.

Figure: 9.1   Aluminium Rod Only

Figure: 9.2   Rod with ADLash

The introduction of ADLash showed the field to be greatly enhanced close to the rod/ ADLash interface as shown in Figure 9.2. The surface stress around the rod surface was calculated by BEM and the results were transferred to a spreadsheet so that the surface could be plotted. The results
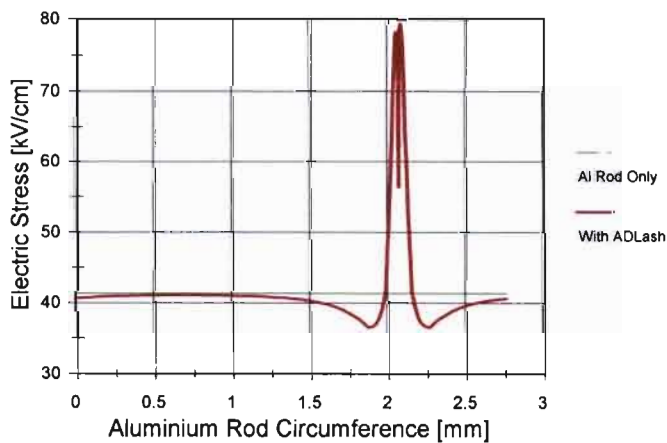
Figure 9.3   Aluminium Surface Stress

are shown in Figure 9.3 and the enhancement of the electric field stress is clearly quantified. BEM

calculated a maximum field stress of G_{MRA} = 79.80 kV/cm. Since the system was simulated as a linear one, the onset voltage with ADLash could be estimated using a simple proportional relationship $V_A = V_R \cdot {G_{MR}}/{G_{MA}} = 84.10$ kV.

9.2 Shield Wire With and Without ADLash

Simulations of the shield wire in the corona cage, with and without ADLash, were done of the shield wire in the corona cage. The field distribution around the aluminium rod was seen to be enhanced around the edges of the individual strands as shown in Figure 9.4. With the applied rod onset voltage of V_S = -162.01 kV, BEM calculated a peak field stress of G_{MS} = 58.11 kVcm^{-1}.
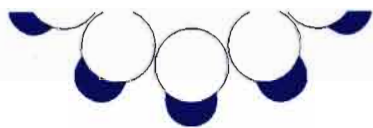
Figure 9.4   Shield Wire Only   **Figure 9.5**   Shield Wire with ADlash
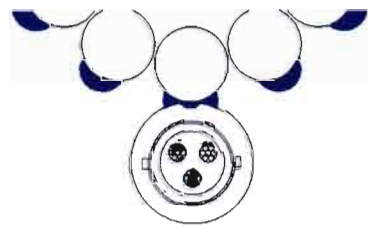
The introduction of ADLash caused the field to be greatly enhanced close to the wire/ ADLash interface as shown in Figure 9.5. The surface stress around the bottom strand surface was calculated by BEM and the results were transferred to a spreadsheet so that the surface could be plotted. The results are shown in Figure 9.6 and the enhancement of the electric field stress is clearly quantified. BEM reported a maximum field stress of G_{MSA} = -136.2 kV/cm. Using the same simple proportional relationship as before, the onset voltages of the shield wire for both cases were calculated. For the shield wire V_S = 115.48 kV and V_{SA} = -49.27 kV. The results of all the simulations are summarised in Table 9.1.
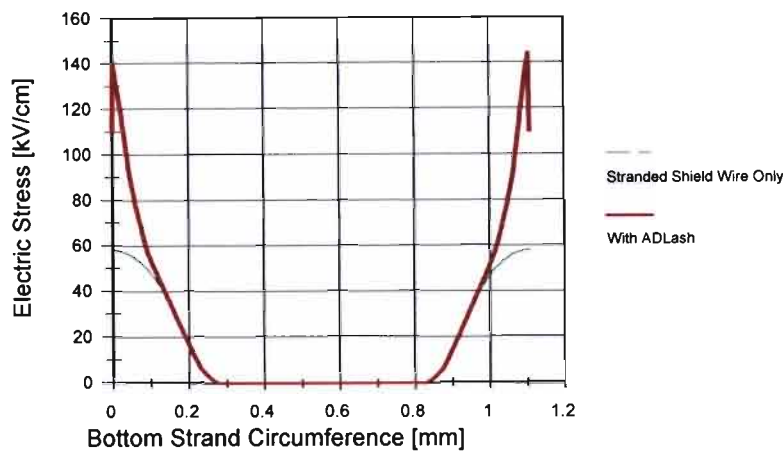
Figure 9.6   Surface Stress Around Bottom Strand

It is clear from these calculations that the introduction of ADLash will theoretically have a

significant impact on the onset voltages at which corona occurs on high voltage conductors. These

Table: 9.1   Effect of ADLASH on Onset Voltages

Conductor	Peak Surface Stress with -162.01 kV applied [kVcm⁻¹]	Estimated Onset Voltage [kV]
Rod only	41.42	-162.01
Rod & ADLash	79.80	-84.10
Shield Wire only	58.11	-115.48
Shield Wire & ADLash	136.20	-49.27

values are compared with actual laboratory tests in Chapter 10. In Figures 9.2 and 9.5 field

enhancements inside the ADLash can be seen, raising the possibility of internal partial discharges.

Chapter 10 Calibration of the HVDC Supply

Calibration of the HVDC supply was carried out before measurements were taken to ensure their accuracy.

Figure: 10.1   Walton Cockroft Voltage Multiplier Circuit

The HVDC centre at the University of Kwazulu-Natal (UKZN) has a two-stage Walton-Cockcroft type DC multiplier circuit as shown in Figure 10.1. It can provide positive or negative voltages up to 500 kV, with a current of up to 7.5 mA with a maximum peak ripple of less than 3 %, [90]. A
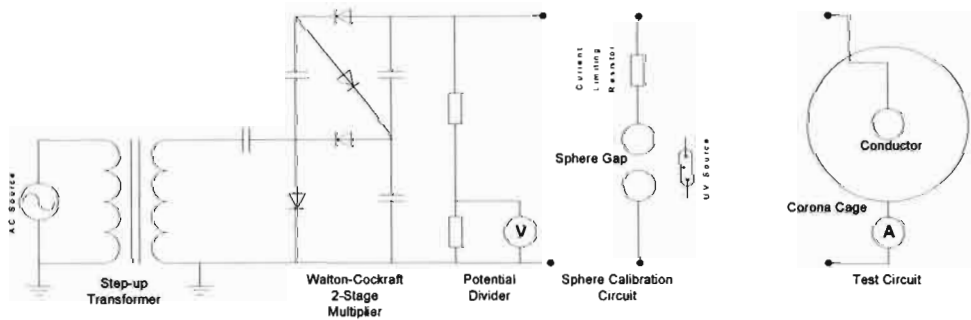
Figure: 10.2   HVDC Supply, Calibration, and Test Circuits

schematic diagram, together with the calibration apparatus and test circuit are given in Figure 10.1.

Measurements of the output voltage are made using an integral voltage potential divider connected to a measurement device such as a voltmeter or oscilloscope.

10.1   Calibration Procedure

Considering the number of components in the circuit, it is essential that the output voltage is calibrated to an internationally acceptable standard. The standard technique for testing high voltage as specified by the Institute of Electrical and Electronic Engineers, (IEEE), [91] is used for the HVDC calibration and measurements.

For the calibration procedure, the HVDC supply is set to give a negative voltage. The main purpose of the calibration procedure is to verify the performance of the potential divider and to determine any correction factor that may be required.

To do this two 10 cm spheres with a gap set at 4 cm are connected to the HVDC source via a current limiting resistor of 10 MΩ as depicted in Figure 10.3. In accordance with the IEEE standard, an ultraviolet source is used to aid ionisation. The IEEE standard does not give flash-over data for 10 cm spheres, but a flash-over voltage of $V_{Table} = 106$ kV at an ambient temperature of

Figure: 10.3   Sphere Spark Gap Apparatus with Series Resistor

25 °C and pressure of 101.3 kPa is given by Naidu and Kamaraju, [92]. This value of flash-over

voltage is affected by the air density, which depends on air temperature, barometric air pressure,

and to a lesser extent, humidity. The IEEE standard lists correction factors for humidity, but Kuffel

et al. [93], note that the effect of humidity is negligible and may be omitted. Consequently the

relative air density factor δ is calculated using only the ambient temperature T (°C), and pressure

P (kPa) as follows:

$$\delta = \frac{P}{101.3} \cdot \left(\frac{273 + 25}{273 + T} \right) \tag{10.1}$$

For the range of temperatures and pressure typically found in the HVDC lab, δ is equal to the air

density correction factor, so the correct flash-over voltage may be calculated as:

$$V_S = V_{Table} \cdot \delta \quad [\text{kV}] \tag{10.2}$$

The calibration process is carried out by applying voltage to the spheres via the current limiting

resistor. The voltage is slowly increased while the voltmeter reading, V_{DC}, of the HVDC supply is

monitored. The voltage is taken as the last value just before the discharge occurs. Immediately

discharge occurs, the voltage is removed to minimise pitting of the sphere surfaces. This is

repeated until at least three successive readings agree to within 3 %. These are averaged and the

peak flash-over voltage is taken to be correct to within 5 %. Since the DC current before flash-over

is much smaller than the HVDC source rated current, the ripple may be regarded as negligible, and

the peak flash-over is taken as being equal to the arithmetic average, or DC value.

10.2   Calibration Results

On the first few attempts, the sphere gap appeared to give spurious results, but it soon settled down

Table: 10.1   Readings on HVDC Voltmeter at Flash-over

Test No.	HVDC Voltmeter Readings [kV]
1	106
2	107
3	106
4	106
Average [V_{DC}]	106.25

and the readings on flash-over are shown in column 2 of Table 10.1.

The temperature was seen to be 101.3 kPa, while the temperature was 22 °C. The voltage according to the spheres was corrected as follows:

$$
\begin{aligned}
V_S &= V_{Table} \cdot \delta \\
&= V_{Table} \cdot \left(\frac{P}{101.3} \cdot \frac{273 + 25}{273 + T} \right) \\
&= 106 \cdot \left(\frac{100.0}{101.3} \cdot \frac{273 + 25}{273 + 22} \right) \\
&= 105.7 \text{ V}
\end{aligned}
\tag{10.3}
$$

The percentage difference between the sphere gap voltage and the error of the HVDC voltmeter was calculated to be

$$
\begin{aligned}
\% \text{ difference} &= \frac{V_S - V_{DC}}{V_{DC}} \cdot 100\% \\
&= \frac{105.7 - 106.25}{106.25} \cdot 100\% \\
&= -0.52\%
\end{aligned}
\tag{10.4}
$$

As was mentioned, the published values of the sphere flash-over voltages are regarded as correct to within 5 %. The percentage difference of -0.52 % was therefore regarded as insignificant and no correction factors were applied to the HVDC source voltmeter readings.

The range of atmospheric temperature and pressure experienced during the tests did not

significantly effect the readings, so no corrections were considered necessary.

Chapter 11 Laboratory Observations of Corona Onset

The variety of ways of estimating the surface stress at which onset of corona occurs, and the lack of certainty on the effects of polarity, made it necessary to observe the onset of corona under various conditions in the HVDC laboratory at the University of Kwazulu-Natal, (UKZN).

First a simple apparatus was constructed to observe the effects of polarity, and then a smooth cylindrical conductor was placed in the corona cage to observe the voltage and hence the surface stress at which corona onset occurs. Observations were then compared with theoretical calculations.

11.1   Effect of Polarity on Corona Onset

The ambiguity of the effect of polarity on the onset of corona on the surface of stranded conductors

Figure: 11.1   Apparatus to Observe Effect of Polarity on Corona Onset

was tested using the simple apparatus illustrated in Figure 11.1. Two samples of stranded

conductor were mounted with the top parts slightly closer to ensure that corona would not occur at the ends. This gave a quasi-parallel conductor arrangement for the observations. For the first test one conductor was earthed and negative voltage was applied to the other. Both conductors were then observed to see which one would experience corona first. To avoid the effects of localised field distortions and other idiosyncrasies of the conductors, the polarities were swopped by earthing the other conductor and applying negative voltage to the first. In both cases corona was first seen on the conductor of negative polarity. This was further confirmed by the fact that the first corona seen had the characteristic spots of negative corona. The voltage was then increased until the characteristic bluish sheath of positive corona was seen on the earthed conductor, which had the relative positive polarity.

The results shown in Table 11.1 demonstrate that corona onset occurs at a slightly lower voltage on the negative conductor in the case of stranded conductors.

Table 11.1 Corona Onset Voltages of Quasi Parallel Conductors.

	Test 1 [kV]	Test 2 [kV]
Negative Conductor	106	109
Earthed Conductor	142	136

11.2 Corona Onset of a Solid Round Conductor

The corona onset and offset voltages of a solid round conductor is tested by placing polished aluminium rods into the corona cage and observing the conductor surface using a Corocam® video camera while adjusting the voltage. This video camera can be used to observe the ultraviolet components of corona that occur before corona is visible to the naked eye.

The *onset voltage* is obtained first by slowly increasing the applied voltage and noting the value when corona is first seen. The voltage is then slowly reduced until the corona just disappears to record the *offset voltage* value.

The results of two sets of tests are presented. The first tests are for a rod of diameter 17.6 mm and the second set is for a rod of diameter 15 mm

11.2.1 17.6 mm Rod Tests

The first rod used was turned down to a diameter of 17.6 mm on a lathe from a larger standard size to give it the same outer diameter as that of the shield wire. It was then polished and placed in the corona cage for testing. The first set of tests was done on 8 December 2004, and the onset and

Table: 11.2   17.6 mm Aluminium Rod Corona Onset Voltages

Supply	Corona Onset Voltages of 1.6 mm Aluminium Rod		
	Test Set A* 8 December 2003	Test Set B* 29 January 2004	Expected Value from Table 5.2
DC [kV]	85 (Offset @ 45.6)	86 (Offset @ 38)	162.01
AC [kV (peak)]	72 (Offset @ 68)	72 (Offset @ 68)	162.01

* Each result represents the average of a number of readings

offset voltage values were noted and compared with the expected values calculated earlier. As shown in Table 11.2, there is a large difference between the observed values of Test Set A and the expected values. Later in Test Set B, cardboard buffers were placed on the ends of the rod to avoid possible quasi-coronas due to the ultra violet that could emanate from the centre conductor clamp, as shown in Figure 11.2. These had no noticeable effect on the onset values.
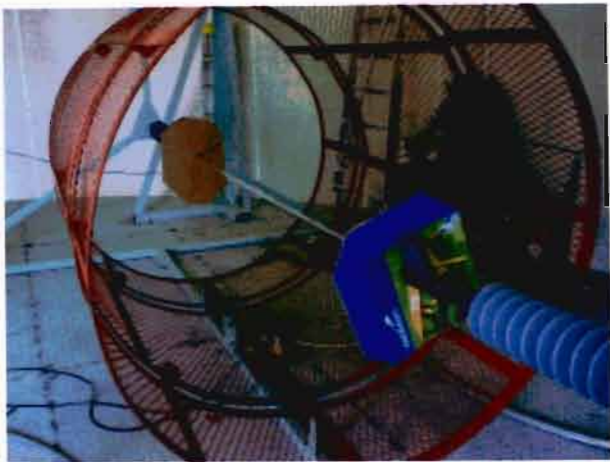
Figure: 11.2   Aluminium Rod in Corona Cage

11.2.1 15 mm Rod Tests

The 17.6 mm rod was carefully inspected and it was noted that its surface was uneven due to the turning process. It also had some scratches. To evaluate the effect of this, a second rod was used, but this one was a standard off-the-shelf size of diameter 15 mm. It was highly polished and placed in the corona cage. Corona onset values were observed using the Corocam camera, and the expected values were calculated using Peek's formula, Equation (5.5). The onset values are higher for a rod with a better surface as is shown in Table 11.3, and are closer to the calculated estimate.

Table: 11.3   15 mm Aluminium Rod Corona Onset Voltages

Supply	Corona Onset Voltages of 15 mm Aluminium Rod	
	Test set C* 29 June 2004	Expected Value from Calculation
DC [kV]	101	140
AC [kV (peak)]	134	140

* Each result represents the average of a number of readings

The AC value is within 5 % of the calculated value regarded as acceptable for high voltage measurements, [94].

11.3   Corona Onset of a Sample of HVDC Shield Wire

The tests as done on the 17.6 mm rod were repeated with a weathered sample of HVDC shield

from the Cahora-Bassa HVDC line and the results are given in Table 11.4 (Test Set D).

Table: 11.4   Stranded Wire Corona Onset Voltages

Supply	Corona Onset Voltages of Shield Wire		
	Test set D* 8 December 2003	Test Set E* 29 January 2004	Expected Value from Table [5.2]
DC [kV]	26 (Offset @ 25.6)	45 (Offset @ 31.5)	118.27
AC [kV (peak)]	24 (-)	33.5 (-)	118.27

* Each result represents the average of a number of readings.

Again the onset and offset values were much lower than the expected values. The wire was

inspected and found to be very dirty. It was thoroughly cleaned and inspected for the next set test.

It was seen that several conductor strands had nicks as seen in Figure 11.3 and abrasions as seen

Figure: 11.3   Nicks in Outer Strands

Figure: 11.4   Abrasions on Outer Strands

in Figure 11.4. Attempts were made to reduce these faults using sandpaper. The shield wire sample

was again tested in January 2004, (Test Set E), where it can be seen that the onset voltages are

noticeably higher, but still much lower than the predicted values.

11.4   Conductors with ADLash

The above tests were repeated with samples of ADLash optical fibre cable lashed first to the

17.6 mm aluminium rod, as illustrated in Figure 11.5, (Test Set F), and then to the shield wire

Table: 11.5   Effect of ADLash on Corona Onset Voltage

Supply	Corona Onset Voltages with ADLash Attached [kV]			
	Rod	Rod & ADLash	SW	SW & ADLash
DC [kV]	86 (38)*	50 (10)	47 (31)	47 (40)
AC [kV peak]	72 (68)	50 (40)	34 (−)	40 (37)

*Brackets indicate offset voltages

sample (Test Set G). The effect of the introduction of the ADLash was to cause the onset of corona

at lower applied voltages on the aluminium rod as illustrated in Table 11.4. The introduction of

the ADLash did not make much difference to the onset voltage value for the stranded conductor

although the corona distribution was very different.

11.5   Comparing Visual Observations

While determining onset and offset values, the corona on the conductors was observed using the

Corocam©. These observations are presented. The Corocam© only provides images in monochrome

with limited resolution, so pictures are first given of the bare aluminium rod, Figure 11.6 and the

stranded shield wire, Figure 11.7 for comparison purposes. Accurate focus is also difficult to

achieve.

Figure: 11.6   Aluminium Rod

Figure: 11.7   Stranded Shield Wire

11.5.1 Corona on 17.6 mm Aluminium Rod

The Aluminium rod was energised with AC, Figure 11.8 and DC, Figure 11.9. From onset to

Figure: 11.8   AC Corona

Figure: 11.9   -ve DC Corona

voltages as high as 200 kV, the distribution was seen to be randomly distributed.

These tests were repeated with samples of the ADLash optical fibre cable lashed to the aluminium

rod. Corona was observed for AC applied voltage, Figure 11.10 and DC applied voltage,

Figure 11.11.The figures show the corona when the applied voltage was quite high, (200 kV) for

clarity. From first onset, the corona was concentrated around the ADLash and particularly around

the bands. With the application of AC voltage, the main source of the corona was from between

Figure: 11.10   AC Corona with ADLash

Figure: 11.11   -ve DC Corona with ADLash

the ADLash and the conductor as expected. However when DC voltage was applied the corona concentrated itself on the bands. Corona on the rest of the conductor was negligible. Increase of applied voltage merely increased the corona intensity and did not cause it to spread. The bands seen in the burst corona of the positive cycle of the AC corona in Figure (10.10) are due to electromagnetic interference from the corona on the computer used to capture the Corocam© images.

11.5.2 Corona on the Stranded Shield Conductor

The stranded shield wire was then placed in the corona cage and observations were made with and

without ADLash attached. AC was first applied and spectacular burst corona was observed on the

conductor surface as depicted in Figure 11.12. Later when the ADLash was fitted to the cable, it

Figure: 11.12   AC Corona
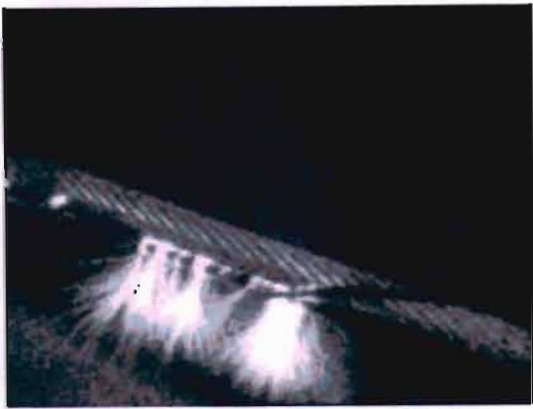
Figure: 11.13   AC Corona with ADLASH

Figure: 11.14   AC Corona with ADLASH
(Lights Off)

was clear that the corona was now concentrated around it. Increasing the voltage increased the

intensity of the corona, but did not cause it to spread onto the surface of the stranded conductor.

The corona remained concentrated on the ADLash, and to a lesser extent on the bands. The same

observations were made with the laboratory lights off, and it was seen that the lighting did not

affect the intensity or distribution of the corona.

Figure: 11.15   DC Corona with ADLASH

Figure: 11.16   DC Corona with ADLash
(Higher Voltage)
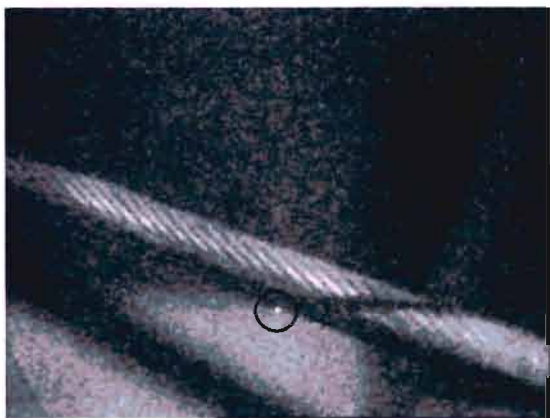
Figure: 11.17   Onset of DC Corona with ADLASH

DC voltage was applied to see the effect on the stranded conductor/ ADLash combination. Now the corona was more concentrated on the bands as shown in Figure 11.15. The corona increased with intensity as the voltage was increased, but did not spread to the conductor surface, as shown in Figure 11.16. The voltage was lowered to determine where the corona starts, and as clearly seen in Figure 11.12, the corona started on the ADLash surface (circled).

Chapter 12 Other Sources of Partial Breakdown

Damage to optic fibre cables is not limited to corona that emanates from the conductor/ ADLash interface. Where optical fibre cables are exposed to electric fields of high enough strength, damage can occur due to dry-band arcing, micro-sparking, and/or corona.

12.1 Dry Band Arcing

No published articles on dry band arcing effecting ADLash have been found, but some research on All Dielectric Self Supporting (ADSS) fibre optic cable done by Tuomein and Olsen is available, [95], [96].

The outer sheath of the ADSS is hydrophobic and non-conductive when new, but becomes
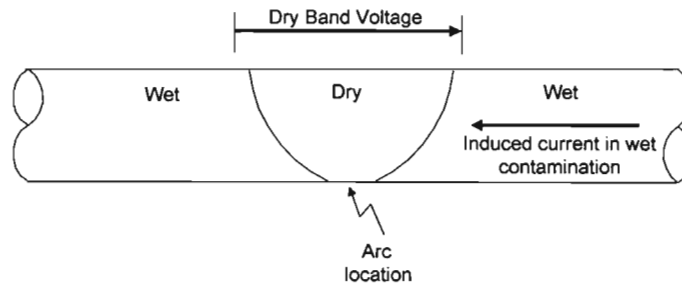
Figure: 12.1   Dry band Arc on ADSS   *(Tuominen & Olsen)*

hydrophilic when old, and will have a layer of pollution on it. With rain the ADSS becomes wet and slightly conductive, having resistance values of 10^5 Ω/m (for heavy pollution), to 10^7 Ω/m (for light pollution). Currents are then induced on the outer sheath from the energised conductors. When dry-bands form, voltages of a few tens of kilovolts occur across them, as illustrated in Figure 12.1. These voltages can cause breakdown of the dry-band, and if the associated currents are high enough, damage can be caused to the ADSS, eventually leading to failure. Tuominen and Olsen describe a model that can be used to predict the dry-band voltages and induced currents.

They quote Bonneville Power Administration as giving 26 kV and 1.5 mA being the values associated with cable sheath damage. Karady, using a similar model, quotes a longitudinal voltage gradient of 11 kV/cm, and an induced current of 1.0 mA to cause damage.

ADLash is lashed to the bottom of the shield wire with bands at a pitch of about 50 cm. The shield wire is specified as having resistance of 247.3 Ω/km and a maximum current rating of 423 A, both at 20°C as given in Appendix B. Assuming a full load current, the longitudinal voltage gradient due to the resistance alone would only be about 1 mV/cm.

The voltage gradient due to the shield wire inductance may be calculated. According to Freeman [97], the inductance of the shield wire may be calculated as follows:

$$
\begin{aligned}
L &= 0.05 + 0.2 \cdot \ln\left(\frac{d}{r_c}\right) \\
&= 0.05 + 0.2\ln\cdot\left(\frac{11.5}{17.6 \cdot 10^{-3}}\right) \\
&= 1.35\,\text{mH/km}
\end{aligned}
\tag{12.1}
$$

where $d = 11.5$ m, the spacing between the shield wire and main conductors, and $r_c = 17.6$ mm, the outer diameter of the shield wire. The main currents are DC and therefore will not contribute to an inductive voltage gradient. The only alternating current of consequence is the carrier signal that has a frequency of 50 kHz [98]. If this current had the impossible value of 423 A, (the current rating of the shield wire), the longitudinal inductive voltage gradient G_{long} would still only be given by (11.2). as follows:

$$
\begin{aligned}
G_{long} &= I \cdot 2\pi fL \\
&= 423 \cdot 2\pi \cdot 50\,000 \cdot 1.35 \cdot 10^{-3} \\
&= 1.8\,\text{kV/cm}
\end{aligned}
\tag{12.2}
$$

This value is still much less than the value of 11 kV/cm, quoted by Karady.

Clearly, the shield wire provides a low impedance path to current where any dry bands may form. The likelihood of any dry-band arcing occurring seems remote.

12.2   Microsparking

Where the surface of the ADLash is hydrophobic, moisture droplets can occur which will cause enhancements in the electric field. This can lead to microsparking and has been observed on ADSS optic fibre cable in a laboratory at the Arizona State University, (ASU), [99]. Further research is required to see if the sparks have enough energy to damage the outer sheath of the optic fibre cables.

12.3   Corona Discharges from Metal Surfaces

Where the surface stress on metal objects such as conductors and fittings is high enough, air in contact with the object surface can breakdown to cause corona onset. This corona can bombard the outer sheath of the optic fibre cable, and slowly erode it to eventually puncture the outer sheath. Water penetration and failure can then occur. The enhancement of surface stress can be caused by one or more of the following:

* shield wire surface stress due to the proximity of the ADLash,

* enhancement of the shield wire surface stress due to micro-projections, and

* corona due to ADLash support assemblies.

12.3.1 Shield Wire Surface Stress due to the Proximity of the ADLash

The higher relative permittivity of the ADLash cable causes enhancements on the shield wire surface stress as well as in the air in the immediate vicinity. This is potentially the main problem facing the use of ADLash and has been dealt with in detail.

12.3.2 Enhancement of the Shield Wire Surface Stress due to Micro-projections

The possibility exists that small projections exist on the shield wire surface. These small projections can be caused by insects on the line, or by small sharp points in the conductor surface due to damage or bad handling during the original cable construction.

This may be quantified by examining the electric stresses with and without a micro-projection on the shield wire surface using the ELECTRO BEM software package. The main conductor voltage is set to the rated value of 533 kV.

The surface stress on the bottom strand of the shield wire and the peak value is calculated to be $G_l = 31.3 \, \text{kVcm}^{-1}$. Figure 12.2 illustrates the surface stress on the bottom strand of the shield wire
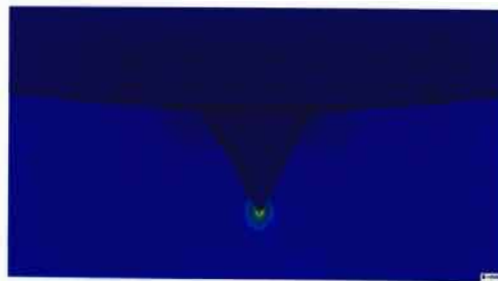
Figure: 12.2   Field Around a Micro-projection on
the Bottom Strand of the Shield Wire

with an equi-triangular micro-projection having side lengths of 0.1 mm. The peak value is calculated to be $G_2 = 132 \text{ kVcm}^{-1}$. This value is merely illustrative. If the field really was this high, the localised heating is likely to melt the sharpness of the point to reduce it to a more realistic value.

It demonstrates however, that the introduction of a micro-projection can enhance the surface stress by about $G_2/G_1 = 4$. As mentioned before, this value is unrealistically high. A more likely value would be about 3, [100].

The corona from insects is not likely to be serious because insects die and dry out within a relatively short time, while the time to cause damage to the optic fibre cable may be as much as 8-15 years, [101].

Corona from sharp points on the surface of the shield wire will be much more permanent and can eventually damage the ADLash cable. Considering the length of the HVDC line, predicting these defects would be impossible and finding and eliminating defects would be difficult.

12.3.3 Corona due to ADLash Support Assemblies

The field conditions along the shield wire are fairly uniform between the towers. The supports at the towers present a completely different picture.

Armour rod assemblies that support ADSS fibre optic cables have been found to cause corona at

the Arizona State University, (ASU), [102] which is illustrated in Figure 12.3.
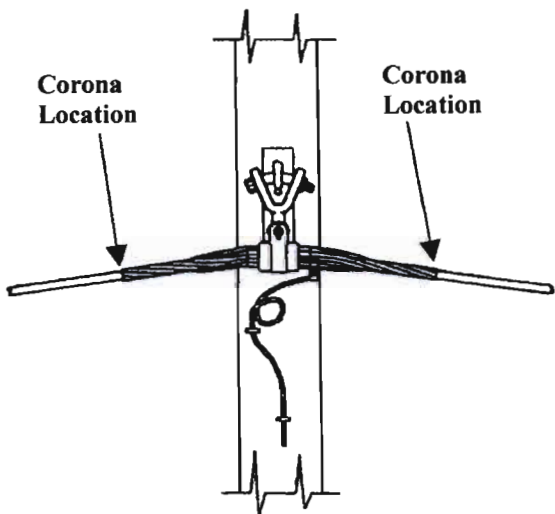
Figure: 12.3   Armour Rod Assembly for ADSS
Fibre-optic Cables   (*ASU*)

Corona develops at the tip of the armour rod assemblies which support the ADSS, and can damage

the outer sheath by erosion as described earlier. It will be necessary to careful design the fittings

that support the shield wire and ADLash at the towers. The corona may be mitigated by using

Figure: 12.4   Avoiding Corona at Insulator Positions   (*Blume*)

corona rings, or nonmetallic supports and fittings, or alternatively it may be avoided by looping

the ADLash as has been done in the fibre wrap installation shown in Figure 12.4, [103]. Clearly,

these three problem areas could damage the ADLash. However, the experience of ADSS is not

directly applicable and further research is required.

-83-

In general, before an optic fibre cable of any type is to be used in any high voltage environment, the effect of the proximity of towers and other fittings on the electric field surrounding the cable needs to needs to be evaluated. Analysis of the field distribution around clamp ends, protrusions and water droplets may reveal significant enhancements, [104]

Chapter 13 Other Suitable Fibre-optic Cable Technologies

Since the application of ADLash to the shield wire is not advisable, it is essential that the suitability or otherwise of other alternative fibres be evaluated. Several different methods of attaching the optic-fibres have been developed, and considering them here briefly is appropriate. These methods include the following:

- all-dielectric self-supporting cables, (ADSS),

- helically-applied fibre-optic cables, (WRAP), and

- optical-groundwire, (OPGW).

These may all be considered as possible alternatives to ADLash and are therefore considered briefly. A good introduction to these is provided by Blume, [105], of which a few pertinent points are discussed here. To choose an optic cable to be retrofitted to the existing HVDC line, ADSS may be the most economical solution in this simple survey, and it is therefore dealt with in some detail.

13.1   All-dielectric Self-supporting Cables, (ADSS)

ADSS is a popular choice that is easily retrofitted to existing installations. As illustrated in Figure 13.1, it is reinforced with aramid fibres and may be hung between overhead lines in positions of minimum voltage gradient. It is available with a semi-conductive sheath to reduce the effects of dry-band arcing.
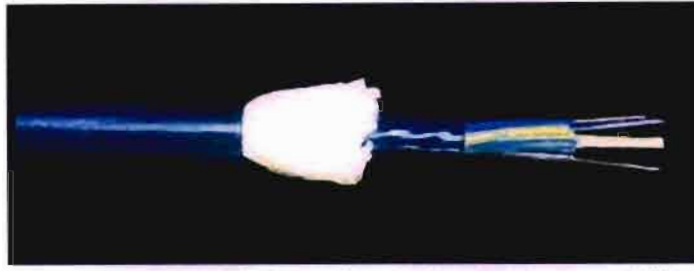
Figure: 13.1   All-dielectric Optic-fibre Cable, showing Aramid Fibres
(Blume)

To predict possible longitudinal voltage gradients that can lead to dry-band arcing, a simple equivalent circuit may be drawn as shown in Figure 13.2, [106]. R represents the pollution layer resistance per unit length, while C_{01} and C_{02} represent the per unit length capacitance of the shield wire/ ADSS, and ADSS/ main conductors respectively.
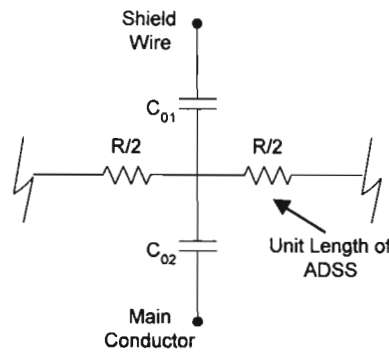
Figure: 13.2   Equivalent Circuit of Unit Length of ADSS
(Karady and Devarajan)

From this model, it can be seen that the longitudinal voltage gradient is primarily due to capacitive coupling. The main conductor current is DC, so the only capacitive coupling that can occur is due either to the HVDC ripple current, or that of the carrier signal. An analysis of these is beyond the scope of this dissertation.

Since both the shield wire and main conductor bundle are mounted on one side of the pylons, it may be acceptable to hang the ADSS on the other side where it will probably be far enough to

minimise coupling effects, (see Appendix A). ADSS seems to be a viable alternative and further

investigation is recommended.

13.2 Helically-Applied Fibre-Optic Cables, (WRAP)

In contrast to taped ADLash, WRAP is wound around the metallic conductor as is illustrated in

Figure 13.3.
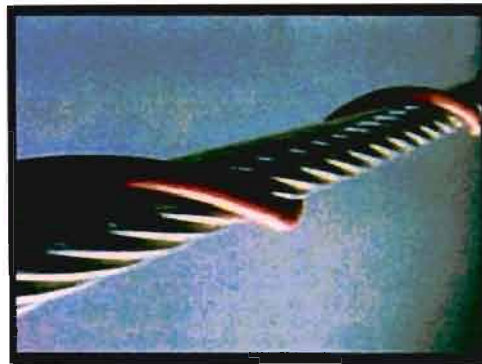
Figure: 13.3   Helically-Applied Fibre-Optic Cable
(Blume)

While a manufacturer of WRAP claims superior electrical and mechanical performance over other

types of optic-fibre cable, [107], its application on an HVDC shield wire does not appear to have

any advantage over ADLash. WRAP is in direct contact with the shield wire and would enhance

the local electric field in the same way that ADLash does. Being helically wound, it also has the

slight disadvantage of requiring about 1.5 % more cable per kilometre, for typical wrapping pitch

lengths and WRAP diameters.

13.3 Optical-Groundwire, (OPGW)

The optical ground wire is a shield wire with the optical fibres fitted in the core providing them
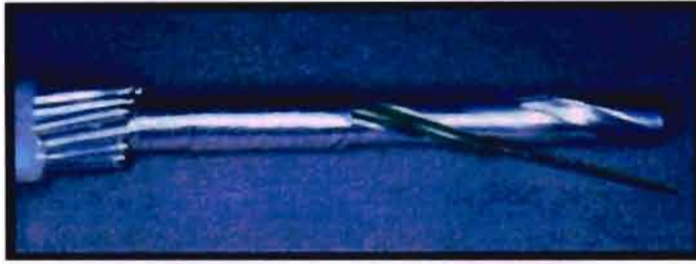
Figure: 13.4   Optical Ground Wire showing Optic Fibres
(*Blume*)

with maximum mechanical protection and electrical shielding as illustrated in Figure 13.4. This is however a very expensive solution because it would mean that the shield wire would have to be replaced along the whole length. OPGW may however be an economical solution worth considering on new installations.

Chapter 14 Conclusion

It has been reported that the HVDC line from Mozambique to South Africa had reliability problems with its powerline carrier communications system and the installation of a fibre optic cable to overcome this is being considered. Different methods of installing fibre optic fibre cables are available but this dissertation is primarily concerned with ADLash retrofitted to existing conductors using bands.

14.1   Published Literature on ADLash

An extensive literature survey has been undertaken for any type of fibre optic cable which is installed in contact with live conductors, but little was found. None of the literature surveyed covered the effect that a fibre optic cable in contact with a live conductor would have on the surrounding electric field. Interpolation had to be used to estimate unknown permittivity values to avoid uncharacteristic field distortions. Indeed the manufacturer of ADLash is unable to supply the permittivity of all the components of the ADLash, indicating that this aspect may not have even been considered.

The EPRI state of the art review of 'Fibre Optic Cables in Overhead Transmission Corridors', expresses the opinion that optic fibre cables which are lashed or clipped to a stranded conductor are obsolete in favour of the types wrapped around a conductor (WRAP), [108].

It is concluded that further research is required for ADLash in high voltage environments.

14.2   Field Plotting Methods

To determine corona onset, determining the stress around conductors is necessary. This was done by plotting the stress. Three methods have been evaluated for their usefulness in studying the electric field surrounding a conductor.

14.2.1 Finite Element Analysis

Quickfield®, a finite element software package, was used in an attempt to simulate a cross section of the HVDC line. The conductors' heights are extremely high when compared with their diameters. Analysis required a very high number of elements that had to be particularly small to cater for the small components of the line conductor strands and the ADLash. Despite many queries to the software support service, useful results could not be obtained.

It has been concluded that the extremely high number of elements required can lead to a proliferation of errors and that the Quickfield program is not suitable for field plotting of high voltage transmission lines.

14.2.2 Boundary Element Method

By defining elements on surfaces, Electro, (a BEM software package), can calculate surface charge densities, potentials etc. It can also plot the electric field stresses on the surfaces or in the space surrounding defined objects. Successful simulations have been presented of the shield wire with and without ADLash attached for both an HVDC line simulation as well as corona cage

simulations. These simulations have been used to predict the onset of corona for given applied voltages.

It is concluded that BEM is an effective tool for analysing the fields around high voltage transmission lines.

ELECTRO however, does not provide the facility to do iterations, and is unable to optimise dimensions such as conductor spacing and heights. Further research to develop a software package that could do this would be very useful.

14.2.3 *Method of Images*

The Method of Images (MI) provides for the analytical calculation of space charge free fields for simple geometries. It is appropriate for cylindrical conductors that are well spaced. By treating the shield wire strands as individual conductors, MI was used to estimate the individual strand surface charge values. These values are shown to agree closely with the charge values calculated using BEM and it is concluded that there is no necessity to procure or develop a software package using MI.

14.3   Published Literature on Corona and Corona Onset

A study of corona discharges was undertaken and while the various modes of corona are well documented, there are diverse views as to exactly what constitutes corona onset and how to predict it. To compound this, researchers have mainly concerned themselves with concentric cylinder and

point-cup configurations that are not directly applicable to stranded conductors. Stranded conductors are extensively used in high voltage power systems, but very little research could be obtained regarding the onset on – or the corona modes peculiar to– stranded conductors for either AC or DC voltages.

It is concluded that a standard definition of corona onset on stranded conductors needs to be agreed on and further research is needed in this regard.

It may be noted that, much of the available literature that covers corona onset, tends to concentrate on the onset stress of almost ideal smooth cylindrical conductors with AC voltage applied. Onset for stranded conductors is then estimated using poorly defined stranding factors. In this dissertation, it has been shown that slight imperfections in the conductor surface can cause the onset value to be markedly lower than that estimated. In particular, once corona onset has occurred on the surface of a DC conductor, it lingers for a long time while the voltage is being reduced.

Clearly the difference between onset and offset voltages demonstrates the effect of photo-ionisation that commences with the onset of corona and aids it while the voltage is being reduced giving a hysteresis effect [109].

14.4 Theoretical and Observed Corona Onset

The voltage at which corona onset occurs was calculated and observed in the HVDC laboratory.

14.4.1 Theoretical Estimates of Corona Onset

The theory of corona onset in concentric cylinders has been presented, together with characteristics of positive and negative corona. The methods for estimating corona onset, as published by seven observers over almost seven decades, are presented and used to predict the onset of corona in the corona cage. These methods are shown to agree closely and assume ideal components without imperfections. It is concluded that the calculation of corona onset in a concentric cylinder configuration is well established.

14.4.2 Laboratory Observations of Corona Onset

To observe the onset of corona, and to compare it with theoretical predictions, the onset of corona in the cage has been examined. The voltage onset for the aluminium rod and shield wire with and without ADLash was estimated. The onset voltages were then observed in the corona cage and compared with the theoretical calculations.

Despite repeated readings with both AC and DC voltages, the observed onset voltages were seen to be much lower than the calculated ones. This needs to be further investigated and further research is required.

For the bare conductors, it is shown that the patterns of corona for AC and DC differed as expected. With the ADLash attached, the distribution of corona differed in a way that is not expected. With AC the corona mainly emanates from between the conductor and the ADLash. With DC corona is confined mainly to the bands.

This shows that the AC corona cannot be seen simply as simple combination of both positive and negative DC coronas as was postulated by early observers such as Peek and others. The effects of space charge surrounding the highly stressed conductor probably cause the difference, but this was not investigated and further research in this regard would be desirable.

14.5   Other Corona Causes

The ADLash/ shield wire interface is not the only location where corona or sparking is expected. It was concluded that micro–sparking due to moisture droplets or micro–projections is possible under conditions explained in the text. Whether these sparks have enough energy to damage the ADLash has not been established, and further research would be required to establish this.

The field distribution and hence the incidence of corona due to the proximity of line fittings such as insulators and line supports has not been evaluated and should be further investigated.

The possibility of dry band arcing was investigated and found unlikely due to the low resistance path of the shield wire in parallel with the ADLash.

14.6   Shield Wire and ADLash

The main concern for ADLash in contact with the shield wire is the fact that corona could damage the ADLash surface. It has been shown that the shield wire surface is close to corona when the main conductors are at rated voltage. Introduction of ADLash can increase the electric stress on the shield wire by about 2.4 times, making corona a certainty. It is concluded that ADLash will

cause corona on the shield wire and field enhancements inside the ADLash risking corona damage

to the ADLash.

14.7   Alternative Fibre Optic Technologies

Since ADLash is not the only available type of fibre optic cable, some alternative types were

reviewed. From the brief survey done, it is concluded that ADSS is more appropriate because it

can be fitted some distance away from the conductors where electric field intensities are much less.

Further research needs to be done to confirm this.

14.8   Final Observation

Various methods were done to evaluate the impact on electric fields of retrofitting ADLash to the

existing Songo–Cahora Bassa HVDC line. It has been shown that the introduction of ADLash will

aggravate the incidence of corona causing an increase in line noise and corona losses and causing

damage to the ADLash outer sheath.

Not withstanding the limits of research noted in this chapter, ADLash cannot be recommended for

use on the HVDC line.

References

1. J. A. Jones, *"Fibre Optic Cables in Overhead Transmission Corridors: A State-of-the-Art Review"*, Electric Power Research Institute TR-108959, pg iii, (Nov 1997)

2. G. C. Sibilant, *"An Introduction to the Cahora Bassa HVDC Scheme and an Investigation into the Effects of Pollution on its Insulators"*, BSc Thesis, University of Cape Town, Appendix B, pg 1, (Nov 1999)

3. D. C. Smith, *"The Telecommunications System Installed on the Apollo-Cahora Bassa HVDC Scheme"*, Transmission Engineering, Eskom, pp.1-4

4. J. A. Jones, *"Fibre Optic Cables in Overhead Transmission Corridors: A State-of-the-Art Review"*, Electric Power Research Institute TR-108959, pg iv, (Nov 1997)

5. A. C. Britten,*"Introduction to Corona in High Voltage AC and DC Transmission Systems"*, Post Graduate Course Notes: HVDC/AC Field Effects and Insulation, pp. 5-9

6. J. A. Jones, *"Fibre Optic Cables in Overhead Transmission Corridors: A State-of-the-Art Review"*, Electric Power Research Institute TR-108959, pg 1-2, (Nov 1997)

7. G. G. Karady, G. Besztercey (Arizona State University, Tempe, AZ, USA), M. Tuominen, *"Corona Caused Deterioration of ADSS Fibre-optic Cables on High Voltage Lines"*, IEEE Transactions, Power Delivery, (USA), vol14, no 4, pp 1438 - 1447, (Oct 1999)

8. F. Kaidanov, R. Munteanu, G. Sheinfain (Israel Electric Corporation Ltd, Haifa, Israel), *"Damages and Destruction of Fibre-optic Cables on 161 kV Overhead Transmission Lines"*, IEEE Electrical Insulation Magazine (USA), vol 16, no 4, pp 16-23, (Jul-Aug 2000)

9. N. M. Moyo, *"Noise Generation Phenomena in the PLC System of the Cahora-Bassa HVDC Transmission Line"*, Postgraduate thesis - University of Durban-Westville University, pp 31-32, (April 2003)

10. C. Horn, R. Girbig, C. R. Gouws, *"All Dielectric Lashed Fibre Optic Cable for Installation on Medium- and High Voltage Power Lines"*, CIGRÉ Southern Africa Regional Conference Proceedings, Session 11, Item 51, (October 2001)

11. G. Gelda, Schneider, L. E. Zaffanela, *"HVDC Transmission Line Reference Book"*, Electric Power Research Institute Technical Report TR-102764, (1993)

12. M. Khalifa, *"High Voltage Engineering"*, Marcel Dekker Inc., ISBN 0-8247-8128-7, (1990)

13. E. Kuffel, W. S. Zaengl, J. Kuffel, *"High Voltage Engineering: Fundamentals"*, Newnes, ISBN 0 7506 3634 3, (2000)

14. F. W. Peek Jr, *"Dielectric Phenomena in High Voltage Engineering"*, McGraw-Hill Book Company Inc, (1929)

15. E. E. Kunhardt, L. H. Luessen, *"Electrical Breakdown and Discharges in Gases"*, Plenum Press, NATO Advanced Science Institutes Series, Volume 89b, ISBN 0-3064-1195-4, (1981)

16. J. D. Cobine, *"Gaseous Conductors - Theory and Engineering Applications "*, Dover Publications, (1957)

17. L. B. Loeb, *"Electrical Coronas - Their Basic Physical Mechanisms"*, University of California Press, Library of Congress Catalogue Card Number 64-18642, (1965)

18. D. B. Phillips, R. G. Olsen, P. D. Pedrow, *"Corona Onset as a Design Optimization Criterion for High Voltage Hardware"*, IEEE Transactions on Dielectrics and Electrical Insulation, Vol. 7, No. 6, December, (2000)

19. V. Cooray, *"The Lightning Flash"*, The Institution of Electrical Engineers, London, United Kingdom, ISBN 0 8529 6780 2, (2003)

20. W. R. Kruesi, *"IEEE Standard Techniques for High-Voltage Testing - 6th edition"*, The Institute of Electrical and Electronics Engineers Incorporated, IEEE Std 4-1978

21. J. A. Jones, *"Fibre Optic Cables in Overhead Transmission Corridors: A State-of-the-Art Review"*, Electric Power Research Institute TR-108959, (Nov 1997)

22. F. W. Peek Jr, *"Dielectric Phenomena in High Voltage Engineering"*, McGraw-Hill Book Company Inc, pp 42-43, (1929)

23. M. Khalifa, *"High Voltage Engineering"*, Marcel Dekker Inc., ISBN 0-8247-8128-7, pg 98, (1990)

24. P. D. Pedrow, Personal Webspace, Washington State University, http://www.eecs.wsu.edu/~pedrow/teaching.htm

25. L. B. Loeb, *"Electrical Coronas - Their Basic Physical Mechanisms"*, University of California Press, Library of Congress Catalogue Card Number 64-18642, pg 5, (1965)

26. E. E. Kunhardt, L. H. Luessen, *"Electrical Breakdown and Discharges in Gases"*, Plenum Press, NATO Advanced Science Institutes Series, Volume 89b, ISBN 0-3064-1195-4, pg 3, (1981)

27. V. Cooray, *"The Lightning Flash"*, The Institution of Electrical Engineers, London, United Kingdom, ISBN 0 8529 6780 2, pg 57, (2003)

28. L. B. Loeb, *"Electrical Coronas - Their Basic Physical Mechanisms"*, University of California Press, Library of Congress Catalogue Card Number 64-18642, pg 8, (1965)

29. E. Kuffel, W. S. Zaengl, J. Kuffel, *"High Voltage Engineering: Fundamentals"*, Newnes, ISBN 0 7506 3634 3, pg 352, (2000)

30. J. O. Bird, *"Higher Electrical Technology"*, Newnes, ISBN 0-7506-2599-6, pg 289, (1996)

31. E. Kuffel, W. S. Zaengl, J. Kuffel, *"High Voltage Engineering: Fundamentals"*, Newnes, ISBN 0 7506 3634 3, pg 297, (2000)

32. E. Kuffel, W. S. Zaengl, J. Kuffel, *"High Voltage Engineering: Fundamentals"*, Newnes, ISBN 0 7506 3634 3, pg 308, (2000)

33. E. Kuffel, W. S. Zaengl, J. Kuffel, *"High Voltage Engineering: Fundamentals"*, Newnes, ISBN 0 7506 3634 3, pg 345, (2000)

34. M. S Maruvada, *"Corona Performance of High-Voltage Transmission Lines"*, Research Studies Press Ltd, ISBN 0 8638 0254 0, pg 67, (2000)

35. V. Cooray, *"The Lightning Flash"*, The Institution of Electrical Engineers, London, United Kingdom, ISBN 0 8529 6780 2, pg 104-105, (2003)

36. D. B. Phillips, R. G. Olsen, P. D. Pedrow, *"Corona Onset as a Design Optimization Criterion for High Voltage Hardware"*, IEEE Transactions on Dielectrics and Electrical Insulation, Vol. 7, No. 6, December, pg 745, (2000)

37. F. W. Peek Jr, *"Dielectric Phenomena in High Voltage Engineering"*, McGraw-Hill Book Company Inc, pp 29, (1929)

38. L. B. Loeb, *"Electrical Coronas - Their Basic Physical Mechanisms"*, University of California Press, Library of Congress Catalogue Card Number 64-18642, pg 3, (1965)

39. F. W. Peek Jr, *"Dielectric Phenomena in High Voltage Engineering"*, McGraw-Hill Book Company Inc, pp 48, (1929)

40. M. P. Sarma, W. Janischewskyj in *"DC Corona on Smooth Conductors in Air - 'Steady State-Analysis of the Ionisation Layer' "*, Proceedings IEE, Vol. 116, pp 161, (January 1969)

41. P. S. Maruvada, *"Corona Performance of High-Voltage Transmission Lines "*, Research Studies Press Ltd, ISBN 0 8638 0254 0, pg 82, (2000)

42. D. B. Phillips, R. G. Olsen, P. D. Pedrow, *"Corona Onset as a Design Optimization Criterion for High Voltage Hardware"*, IEEE Transactions on Dielectrics and Electrical Insulation, Vol. 7, No. 6, December, pg 746, (2000)

43.   D. B. Phillips, R. G. Olsen, P. D. Pedrow, *"Corona Onset as a Design Optimization Criterion for High Voltage Hardware"*, IEEE Transactions on Dielectrics and Electrical Insulation, Vol. 7, No. 6, December, pg 749, (2000)

44.   A. C. Britten, C. Van der Merwe, *"Eskom's Corona Cage as a Tool for Research into Corona Phenomena at High Altitudes"*, Class Notes HVDC Systems Design and Operation, pp 45-52, (2002)

45.   G. Gelda, Schneider, L. E. Zaffanela, *"HVDC Transmission Line Reference Book"*, Electric Power Research Institute Technical Report TR-102764, pp 3.18-19, (1993)

46.   F. W. Peek jr, *"Dielectric Phenomena in High-Voltage Engineering"*, McGraw-Hill Book Company, 3rd edition, pp 57-59, (1929)

47.   E. Kuffel, W. S. Zaengl, J. Kuffel, *"High Voltage Engineering: Fundamentals"*, Newnes, ISBN 0 7506 3634 3, pg 345, (2000)

48.   F. W. Peek jr, *"Dielectric Phenomena in High-Voltage Engineering"*, McGraw-Hill Book Company, 3rd edition, pp 396, (1929)

49.   V. Cooray, *"The Lightning Flash"*, The Institution of Electrical Engineers, London, United Kingdom, ISBN 0 8529 6780 2, pg 119, (2003)

50.   L. B. Loeb, *"Electrical Coronas - Their Basic Physical Mechanisms"*, University of California Press, Library of Congress Catalogue Card Number 64-18642, pg 74, (1965)

51.   L. B. Loeb, *"Electrical Coronas - Their Basic Physical Mechanisms"*, University of California Press, Library of Congress Catalogue Card Number 64-18642, pp 2-3, (1965)

52.   J. W. Whitehead, *"High Voltage Corona - International Critical Tables"*, McGraw-Hill, (1929), as quoted by M. P. Sarma, W. Janischewskyj in *"DC Corona on Smooth Conductors in Air - 'Steady State-Analysis of the Ionisation Layer' "*, Proceedings IEE, Vol. 116, pg164, January (1969)

53.   F. G. Heymann, *"Corona on Wires in Air"*, Transaction of South African Institute of Electrical Engineers, Vol 56, Part 11, pp 271-290, (November 1965)

54.   F. G. Heymann, *"Corona on Wires in Air"*, Transaction of South African Institute of Electrical Engineers, Vol 56, Part 11, pg 286, (November 1965)

55.   M. P. Sarma, W. Janischewskyj in *"DC Corona on Smooth Conductors in Air - 'Steady State-Analysis of the Ionisation Layer' "*, Proceedings IEE, Vol. 116, pp 165-166, (January 1969)

56.   M. Khalifa, *"High-Voltage Engineering - Theory and Practice"*, Marcel Dekker Incorporated, ISBN 0 8247 8128 7, pp 133-135, (1990)

57.   M. Khalifa, *"High Voltage Engineering"*, Marcel Dekker Inc., ISBN 0-8247-8128-7, pg 133 (1990)

58. E. Kuffel, W. S. Zaengl, J. Kuffel, *"High Voltage Engineering: Fundamentals"*, Newnes, ISBN 0 7506 3634 3, pg 342-345, (2000)

59. P. D. Pedrow, R. G. Olsen, *"Corona Streamer Onset as an Optimisation Criterion for Design of High Voltage Hardware on Transmission Lines"*, IEEE International Symposium on Electrical Insulation, Montreal, Quebec, Canada, pp312-315, (16-19 June 1996)

60. M. P. Sarma, W. Janischewskyj, *"DC Corona on Smooth Conductors in Air"*, Proceedings IEE, Vol. 116, No. 1, pg 164, (January 1996)

61. D. B. Phillips, R. G. Olsen, P. D. Pedrow, *"Corona Streamer onset as a Design Optimization Criterion for High Voltage Hardware"*, IEEE Transactions on Dielectrics and Electrical Insulation, pp 744-751, (December 2000)

62. E. E. Kunhardt, L. H. Luessen, *"Electrical Breakdown and Discharges in Gases - Part B"*, Plenum Press, ISBN 0 3064 1194 6, pg 7, (1981)

63. E. E. Kunhardt, L. H. Luessen, *"Electrical Breakdown and Discharges in Gases - Part B"*, Plenum Press, ISBN 0 3064 1194 6, pg 7, (1981)

64. M. Khalifa, *"High-Voltage Engineering - Theory and Practice"*, Marcel Dekker Incorporated, ISBN 0 8247 8128 7, pp 135, (1990)

65. J. D. Cobine, *"Gaseous Conductors - Theory and Engineering Applications "*, Dover Publications, pp 256, (1957)

66. G. C. Sibilant, A. C. Britten, N. M. Ijumba, *"Studies of DC Conductor Corona in a Small Corona Cage"*, University of Durban Westville, pg 2

67. Matlab®, Version 5.2, The MathWorks Incorporated, March 1998

68. Siemens Aktiengesellschaft, *"Electrical Engineering Handbook"*, Siemens AG, ISBN 3 8009 1076 4, pg 133, (1981)

69. J. S. Carroll, B. Cozzens, as discussed by W. S. Peterson *"[AC] Transmission Lines to Operate at Voltages Between 220 kV and 330 kV "*, American Institute of Electrical Engineers, pg 63, (March 1933)

70. M. Khalifa, *"High Voltage Engineering"*, Marcel Dekker Inc., ISBN 0-8247-8128-7, pp 11-20 (1990)

71. G. Geisecke, *"Electrical Engineering Handbook"*, Siemens, pg 43 (1981)

72. Hewlett Packard, *"HP 48G Series User's Guide"*, HP Part No. 00048-90126, pg 25-12 (1994)

73. G. Gelda, Schneider, L. E. Zaffanela, *"HVDC Transmission Line Reference Book"*, Electric Power Research Institute Technical Report TR-102764, pg 1.36 (1993)

74. G. Gelda, Schneider, L. E. Zaffanela, "*HVDC Transmission Line Reference Book*", Electric Power Research Institute Technical Report TR-102764, pg 1.35 (1993)

75. Corel Quattro Pro, Version 8, COREL CORPORATION LIMITED, Copyright © 1997

76. S. R. Knutson, M. D. Abdalla, R. M. Pixton, "*PC-Based Electrostatic Field Calculation Techniques*", 12th Annual Ideas in Science and Electronics Exposition/ Symposium, pg 167 (May 1991)

77. S. R. Knutson, M. D. Abdalla, R. M. Pixton, "*PC-Based Electrostatic Field Calculation Techniques*", 12th Annual Ideas in Science and Electronics Exposition/ Symposium, pg 168 (May 1991)

78. S. R. Knutson, M. D. Abdalla, R. M. Pixton, "*PC-Based Electrostatic Field Calculation Techniques*", 12th Annual Ideas in Science and Electronics Exposition/ Symposium, pg 166-171 (May 1991)

79. Y. Bulent Yildir, "*Computer-Aided Field Analysis of High Voltage Apparatus Using the Boundary Element Method*", Proceedings of the International Coil Winding Conference, Rosemont, Illinois, pg 42-48 (October, 1987)

80. ELECTRO Version 6, Two-Dimensional, Rotational-Symmetric, Electrostatic Field Solver, Integrated Engineering Software, (January, 2003)

81. ELECTRO Quick Start Guide, ELECTRO Version 6, Two-Dimensional, Rotational-Symmetric, Electrostatic Field Solver, Integrated Engineering Software, pg 5-6, (January, 2003)

82. N. M. Moyo, "*Noise Generation Phenomena in the PLC System of the Cahora Bassa HVDC Transmission Lines*", Post-graduate Thesis, University of Durban Westville, pg 37-38 (April, 2003)

83. Gelda, Schneider, Zaffanela, "*HVDC Transmission Line Reference Book*", Electric Power Research Institute Technical Report TR-102764, pg 1.37 (1993)

84. F. W. Peek jr, "*Dielectric Phenomena in High-Voltage Engineering*", McGraw-Hill Book Company, 3rd edition, pp 73, (1929)

85. M. Moreno, A. Pigini, F.Rizk, "*Influence of Air Density on the Dielectric Strength of External Insulation*", Guidelines for the Evaluation of the Dielectric Strength of External Insulation, Cigré WG 33.07, pg 59

86. G. C. Sibilant, "*A Study of High Voltage Direct Current Conductor Corona in a Purpose Built Corona Cage*", Masters Thesis, University of Durban-Westville, Appendix B: General Specifications of the Line, (2003)

87. J. S. Carroll, B. Cozzens, as discussed by W. S. Peterson "*[AC] Transmission Lines to Operate at Voltages Between 220 kV and 330 kV* ", American Institute of Electrical Engineers, pg 63, (March 1933)

88. M. S. Naidu, V. Kamaraju, *"High Voltage Engineering"*, McGraw-Hill, Second edition, ISBN 0-07-462286-2, pg 8 (1995)

89. M. S. Naidu, V. Kamaraju, *"High Voltage Engineering"*, McGraw-Hill, Second edition, ISBN 0-07-462286-2, pg 9 (1995)

90. Instruction Manual for 500 kV Test Set, MWB (India) Ltd Bangalore, Pg 6

91. W. R. Kruesi, *"IEEE Standard Techniques for High-Voltage Testing - 6th edition"*, The Institute of Electrical and Electronics Engineers Incorporated, IEEE Std 4-1978

92. M. S. Naidu, V. Kamaraju, *"High Voltage Engineering - 2nd Edition"*, McGraw-Hill, ISBN 0-07-462286-2, pg 178, (1995)

93. E. Kuffel, W. S. Zaengl, J. Kuffel, *"High Voltage Engineering: Fundamentals - 2nd edition"*, Newnes, ISBN 0-7506-3634 3, pg 88, (2000)

94. W. R. Kruesi, *"IEEE Standard Techniques for High-Voltage Testing - 6th edition"*, The Institute of Electrical and Electronics Engineers Incorporated, IEEE Std 4-1978

95. M. W. Tuominen, R. G. Olsen, *"Electrical Design Parameters of All-Dielectric-Self-Supporting Fibre Optic Cable"*, IEEE Transactions on Power Delivery, Vol 15, No. 3, (July 2000)

96. G. G. Karady, S. Devarajan, *"Algorithm to Predict Dry-Band Arcing in Fibre-Optic Cables "*, IEEE Transactions on Power Delivery, Vol 16, No. 2, (April 2001)

97. P. J. Freeman, *"Electric Power Transmission & Distribution - 2nd edition "*, George Harrap & Co., ISBN 0-2455-2449-5 , Pg 176, (1968)

98. A. C. Britten, Verbal Confirmation

99. G. G. Karady, G. Besztercey, *"Corona Caused Deterioration of ADSS Fibre-Optic Cables on High Voltage Lines"*, IEEE Transactions on Power Delivery, Vol 14, No. 4, pg 1439, (October 1999)

100. D. Hoch, *"Class Notes, High Voltage Engineering IV"*, Natal University

101. G. G. Karady, G. Besztercey, *"Corona Caused Deterioration of ADSS Fibre-Optic Cables on High Voltage Lines"*, IEEE Transactions on Power Delivery, Vol 14, No. 4, pg 1443, (October 1999)

102. G. G. Karady, G. Besztercey, *"Corona Caused Deterioration of ADSS Fibre-Optic Cables on High Voltage Lines"*, IEEE Transactions on Power Delivery, Vol 14, No. 4, pg 1438, (October 1999)

103. S. W. Blume, *"Power Play - Utilities Offer Cable Systems New Fibre Options"*, Communications Technology, PBI Media's Broadband Group, pg 3, (April 1999)

104. B. Florkowska, A. Jackowicz-Korczyński, M. Timler, R. Wlodek, *"Analysis of Electric Field Distribution Around the High-Voltage Overhead Transmission Lines with an ADSS Fibre Optic Cable"*, University of Science and Technology, Cracow, Poland

105. S. W. Blume, *"Power Play - Utilities Offer Cable Systems New Fibre Options"*, Article in Communications Technology, PBI Media's Broadband Group, pg 3, (April 1999)

106. G. G. Karady, S. Devarajan, *"Algorithm to Predict Dry-Band Arcing in Fibre-Optic Cables "*, IEEE Transactions on Power Delivery, Vol 16, No. 2, pg 286, (April 2001)

107. H. Ito, T. Takahashi, Y. Namekawa, H. Takagi, *"Development of Thermo-resistant Wrap-on Type OPGW"*, Hitachi Cable Review, No. 18, pp 13-18, (October 1999)

108. J. A. Jones, *"Fibre Optic Cables in Overhead Transmission Corridors: A State-of-the-Art Review"*, Electric Power Research Institute TR-108959, pg 1-3, (Nov 1997)

109. H. J. Ryan, H. H. Henline, *"The Hysteresis Character of Corona Formation"*, AIEE Transactions, pp 1118-1124, (October 1924)

Appendix A

HVDC Line Conductor Configuration

- Shield wire attachment from ground h_e = 36.7 m.
- Conductor attachment above ground h_c = 25.8 m.
- Height between conductor and shield wire is 10.9 m.
- Horizontal distance between conductor and shield wire is 3.6 m.
- Distance between centres of shield wire and conductor is 11.48 m.
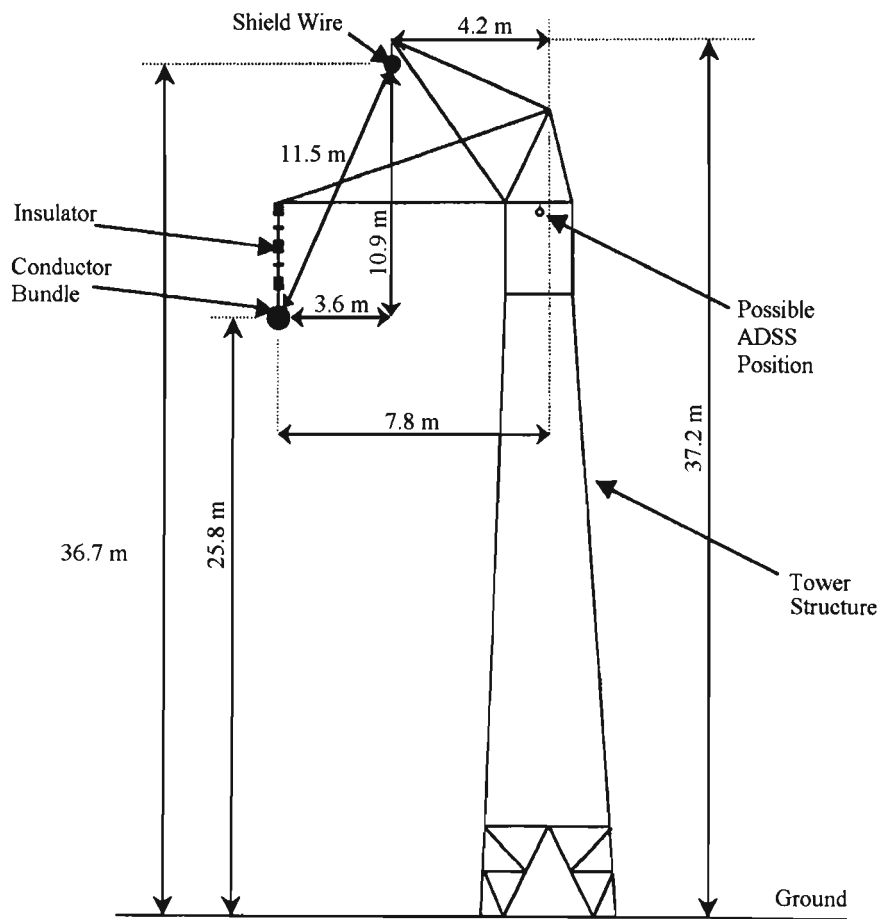- Sag between towers is nominally 16 m.

Figure: A1   HVDC Tower Dimensions   *(Moyo)*

ABERDARE CABLES (PTY.) LTD.

TECHNICAL DATA SHEET

ACSR

DESIGN CODE : 050189		Date of Issue:	13/06/01

Unless otherwise stated all Dimensions are Nominal and are subject to Manufacturing Tolerances.

Code Name	ODEN	CONDUCTOR
Specification	BS 215/70	DETAILS
Stranding and Wire Diameters	12/7/3.52	mm
Diameter over Steel	10.56	mm
Overall Diameter	17.60	mm
Strand Build-up	1-6 St + 12 Al	
Type of Grease	N/A	
Grease Drop Point	N/A	°C
Aluminium Area	116.78	mm²
Steel Area	68.12	mm²
Total Area	184.90	mm²
Aluminium Mass	323	kg/km
Steel Mass	547	kg/km
Grease Mass	N/A	kg/km
Total Mass	870	kg/km
D.C. Resistance at 20°C	0.2473	ohm/km
Ultimate Tensile Strength	94540	Newtons
Breaking Load	9647	kg
Coefficient of Linear Expansion	16.57	per °C * 10⁻⁶
Initial Modulus of Elasticity	69300	N/mm²
Final Modulus of Elasticity	108000	N/mm²
Current Rating (as per Operating Conditions stated belo	423	A

OPERATING CONDITIONS

Operating temperature.	75	°C
Ambient Temperature.	25	°C
Wind Speed.	0.44	m/s
Solar Radiation.	0.089	W/cm²

DRUM DETAILS

Standard Length	2500	m
Diameter over Flange Batterns	1526	mm
Overall Drum Width	976	mm
Gross Mass	2440	kg
Material	WOOD (S.A. Pine)	
Treated (i.e. resistant against biological attack).	No	

DISCLAIMER. Every effort has been made to ensure the information contained on this data sheet is correct. Aberdare disclaim responsibility for any action , proceedings , liabilities , claims , damages , costs , losses and expense in relation to or arising out of incorrect utilisation of this information. Aberdare reserves the right to make changes to this data as and when required.

PREPARED BY TECHNICAL DESIGN DEPARTMENT , PORT ELIZABETH

ABERDARE CABLES (PTY.) LTD.

TECHNICAL DATA SHEET

ACSR

DESIGN COD 050314	Date of Issue:	13 06 01

Unless otherwise stated all Dimensions are Nominal and are subject to Manufacturing Tolerances.

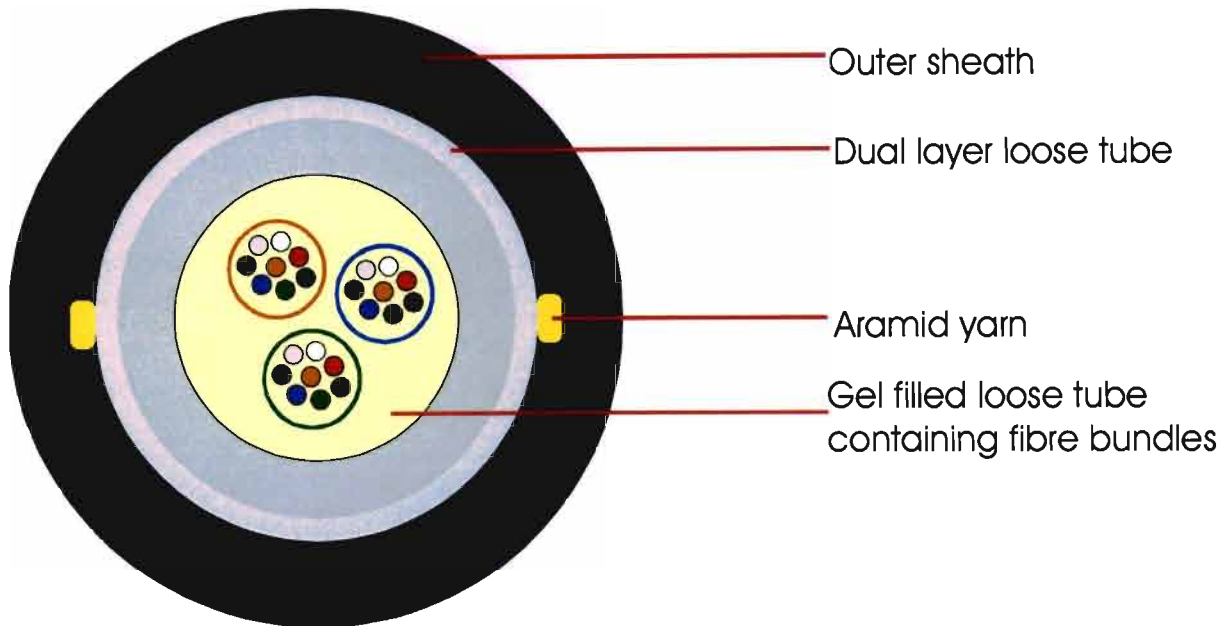| Code Name	ZAMBEZI	CONDUCTOR
Specification	BS 215/70	DETAILS
Stranding and Wire Diameters	42/4.14 + 7/2.32	mm
Diameter over Steel	6.96	mm
Overall Diameter	31.80	mm
Strand Build-up	1-6 St + 8-14-20 AL	
Type of Grease	N/A	
Grease Drop Point	N/A	°C
Aluminium Area	565.38	mm²
Steel Area	29.59	mm²
Total Area	594.97	mm²
Aluminium Mass	1561.00	kg/km
Steel Mass	239.00	kg/km
Grease Mass	N/A	kg/km
Total Mass	1800.00	kg/km
D.C. Resistance at 20°C	0.0511	ohm/km
Ultimate Tensile Strength	125250	Newtons
Breaking Load	12780	kg
Coefficient of Linear Expansion	21.21	per °C * 10⁻⁶
Initial Modulus of Elasticity	40800	N/mm²
Final Modulus of Elasticity	64700	N/mm²
Current Rating (as per Operating Conditions s	1074	A

Conductor - Black and Exposed to Sun	OPERATING CONDITIONS	
Operating temperature.	75	°C
Ambient Temperature.	25	°C
Wind Speed.	0.44	m/s
Solar Radiation.	0.089	W/cm²

DRUM DETAILS

Standard Length	1000	m
Diameter over Flange Batterns	1876	mm
Overall Drum Width	1066	mm
Gross Mass	2190	kg
Material	WOOD (S.A. Pine)	
Treated (i.e. resistant against biological attack).	No	

DISCLAIMER. Every effort has been made to ensure the information contained on this data sheet is correct. Aberdare disclaim responsibility for any action , proceedings , liabilities , claims , damages , costs , losses and expense in relation to or arising out of incorrect utilisation of this information. Aberdare reserves the right to make changes to this data as and when required.

PREPARED BY TECHNICAL DESIGN DEPARTMENT , PORT ELIZABETH

Outer sheath

Dual layer loose tube

Aramid yarn

Gel filled loose tube containing fibre bundles

Application

Due to the non-metallic construction these cables are suitable for installation on earth wires in the vicinity of any system voltage.

Features

- 24 fibres
- The central layout of the fibres allows an inexpensive and small cable build-up.
- The loose tube technology allows the fibres a measure of free movement in the tube which keeps the fibres stress free while the cable is subjected to longitudinal and environmental stress as well as vibration.
- Long outdoor life due to a U.V. protected outer sheath.
- The cable is metal free and therefor immune to radio frequency interference (RFI) and electromagnetic interference (EMI).
- Not affected by electrostatic discharge
- The absence of induced voltages eliminates safety risks to personnel and equipment
- Easy splicing
- Hydrogen absorption is virtually eliminated by means of the gel in the tube, super absorbent polymer technology as well as the loose tube and sheathing materials.

ABERDARE

24 FIBRE CABLE TO ESKOM SPECIFICATION TSP0319

FIBRE OPTIC CABLES

Cable construction

Fibres
Corning SMF28 single mode fibres which have a dual layer acrylic primary coating.
Fibres are individually coloured by means of U.V. cured ink for ease of identification, mechanical stripping of the fibres using Millar type strippers is recommended.
The nominal diameter over the coloured fibre is 0.25mm.
Fibre colours   :   Blue, orange, green, brown, grey, white, red, black.

Fibre bundles
8 Coloured fibres make up a fibre bundle, the three fibre bundles are identified by means of a blue, orange and green binder respectively.
The nominal bundle diameter is 0.84mm.

Loose tube
The centrally situated loose tube is a dual layer polycarbonate/polyethylene and is filled with a non toxic and dermatological safe gel compound and contains 3 * 8 fibre bundles.
The nominal dimensions of the tube is 3.10mm / 3.90mm / 4.10mm.
The permitivity of the polycarbonate is 3.00 and that of the polyethylene is 2.30.

Strength elements
Longitudinal strength is achieved by means of aramid yarns.

Cable sheath
Black U.V. resistant medium density polyethylene sheath. The permittivity of the sheath is 2.55.

Properties

Fibre count	24
Cable diameter (mm)	5.9
Cable mass (kg/km)	30
Number of fibres per bundle	8
Number of fibre bundles	3
Minimum bending radius (mm)	130
External drum dimensions (mm)	630 high / 465 wide
Shipping mass (kg)	74
Standard cable length	2000m

Cable performance and inspection

Parameter	Conditions	Method	Pass criteria
Mechanical performance			
Tensile	100N	IEC 794-1-E1	Fibre strain shall not exceed 0.20%
Crush resistance	1000 N/10 cm, 100 mm * 100 mm plate – 60 seconds	IEC 794-1-E3	The fibre or component parts of the cable shall not suffer any permanent damage. No damage or attenuation change after 1 minute test.
Impact resistance	3 * 1 Nm blow, 300 mm anvil	IEC 794-1-E4	No change in optical fibre transmission properties.
Resistance to water penetration	3m length of cable, 1m head of water containing water soluble fluorescent dye.	IEC 794 – 1 – F5, test method 5B	No dye evident under an ultraviolet light after 24 hrs @ 20±5°C.
Environmental	Cold cycle : -20°C, hot cycle : +70°C, 5 * 24 hr cycles.	IEC 794-1-F1	Attenuation change shall not exceed 0.1 dB/km from the mean over the last four cycles.
Cable bending	Wrap / unwrap cable 4 turns for 10 cycles around a mandrel of 130 mm diameter	In house	The fibre or component parts of the cable shall not suffer any permanent damage.
Cable twist (Torsion)	1m sample subjected to a full clockwise twist followed by two anti clockwise twists.	IEC 794-1-E7	The fibre or component parts of the cable shall not suffer any permanent damage.
Aeolian vibration	Clause 8.2.9 of Eskom specification TSP 0319	Clause 8.2.9 of Eskom specification TSP 0319	Clause 8.2.9 of Eskom specification TSP 0319
Simulation of short circuit currents	Clause 8.2.7 of Eskom specification TSP 0319	Clause 8.2.7 of Eskom specification TSP 0319	Clause 8.2.7 of Eskom specification TSP 0319
Lightning impact simulation	Clause 8.2.8 of Eskom specification TSP 0319	Clause 8.2.8 of Eskom specification TSP 0319	Clause 8.2.8 of Eskom specification TSP 0319
Optical performance			
Attenuation	Backscattering technique	IEC 793-1-C1C	G652 Fibre ≤0.35dB/km @ 1310nm ≤0.20dB/km @ 1550nm G655 Fibre ≤0.25dB/km @ 1550nm ≤0.25dB/km @ 1625nm

Visual inspection

Dimensional, colouring (fibres / tubes / sheath in accordance with BS 6746C colour chart) and cable identification

- Mechanical inspection shall be carried out at a frequency to be agreed between purchaser and supplier.
- Certified test results will be supplied with each drum
- If testing and inspection is required to be carried out by a third party, such parties will be nominated and paid by the purchaser
- Any testing requirements not covered in this specification sheet are subject to discussion and agreement between the supplier and the purchaser.
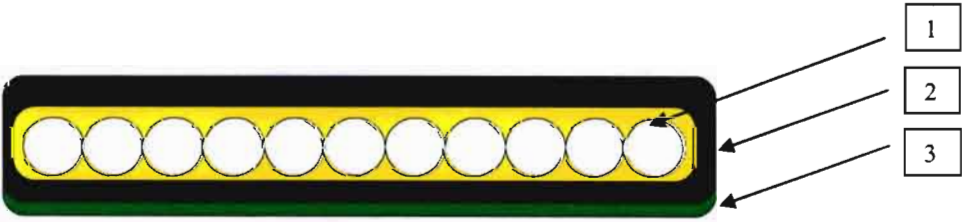- Unless otherwise specified all values in this specification sheet are nominal.

Purchase codes

G652 Fibre   :   392408

CORNING
Discovering Beyond Imagination

Data Sheet of AD-Lashing Band

Product Description
Special construction with excellent long-term performance. The sheath is made of a cross-linked cable material with expected service lifetime of more than 25 years. Resistant to UV light and humid environments. Glass yarns provide tensile strength with long-term stability. An inner layer adheres yarns to the jacket and provides protection against water penetration. Short term temperature resistance up to 300 °C:

Typical Applications
Lashing of AD cables to ground wires and phase wire up to 30 kV line votage

Dimensions		
Width: 4 mm	Thickness: 1.2 mm	Delivery length: max. 1100 m

Technical Data

1. Carrier: glass yarns with melt glue
2. Jacketing: cross-linked cable sheathing material
3. Layer: anti skid layer for shock resistance on the coil

Technical Values
Black U.V. resistant medium density polyethylene sheath. The permittivity of the sheath is 2.55

Matlab Formula to Calculate Corona Onset Stress

```
% This program calculates the corona onset levels for
% a smooth cylindrical conductor inside a concentric cylinder
% using 6 different methods:
%
% Peek's formula
% Whitehead's formula
% Heymann's formula
% Khalifa's formula
% Washington State University Corona Onset Criterion
clear all
echo off

% Enter calculation parameters
rc=.88;        %Conductor radius [cm]
R=75;          %Outer cylinder radius [cm]
P=101.3;       %Atmospheric Pressure [kPa]
T=20;          %Ambient temperature  [deg C]
%
%Calculate Air Density Factor (airden)
airden=P/101.3*(293/(273+T));
%
% Peek's formula calculation
Gpeek=31*airden*(1+0.308/sqrt(airden*rc));
Gcond(1,1)=Gpeek;
Vpeek=Gpeek*rc*log(R/rc);
%
% Whitehead's Formula
Gcond(2,1)=33.7*airden+8.13*sqrt(airden/rc);
Gcond(3,1)=31.02*airden+9.54*sqrt(airden/rc);
%
% Heymann's Formula
Gcond(4,1)=24-3.3+14.2*(rc*airden)^-0.4;
Gcond(5,1)=24+3.3+14.2*(rc*airden)^-0.4;
%
%Khalifa's Formula
A=[31;39.8;29.4;40.3];
B=[11.8;8.4;9.9;7.3];
for x=1:4
   Gcond(x+5,1)=A(x)*airden+B(x)*sqrt(airden/rc);
   end
%
% Zaengl & Nyffenegger's formula
G0=24.36;                 % Constant set by Zaengl & Nyffenegger
Gzaengl=1.2*Gpeek;        %Choose initial LOW value for Gzaengl
                          %based on Peek's value
while (Gzaengl/airden)^2-2*G0*Gzaengl/airden*log(Gzaengl/G0/airden)-
G0^2>42/airden/rc
   Gzaengl=Gzaengl*0.9999;
end
Gcond(10,1)=Gzaengl;
%
```

```
% Washington State University (WSU) Criterion

%Find the radius and stress at ionisation limit
G0=1.2*Gpeek;            %Choose initial HIGH value for onset stress G0
%                        based on Peek's calculation
ion=2;                   %Dummy value
att=1;                   %Dummy value
while ion>att            %Defines ionisation zone
   G0=G0*0.9999;         %Decrease G0
   ion=airden*3632*exp(-168*airden/G0);
   att=airden*(9.9865-(0.541e-3)*(G0/airden)+(1.118e-8) *(G0/airden)^2);
end
V=1.2*Vpeek;             %Choose initial HIGH value for applied voltage V
%                        based on Peek's calculation

N=3501;                                 %Dummy value of exit criterion
while N>3500;                           %WSU corona onset criterion
   V=V*0.9999;                 %Decrease V
   r0=V/(G0*log(R/rc)); %Radius of ionisation limit for V
   dr=(r0-rc)/100;             %Calculate integration interval
      N=0;                        %Reset N
   evens=0;                    %Reset sum of even coordinates
   odds=0;                     %Reset sum of odd coordinates
   for m=0:500;
      r=rc+m*dr;
      G=V/(r*log(R/rc));
            ion=airden*3632*exp(-168*airden/G);
      att=airden*(9.9865-(0.541e-3)*(G/airden)+(1.118e-8) *(G/airden)^2);
      ion_minus_att=ion-att;
      if m==0
         start_value=ion_minus_att; %Save start value
      elseif m==500
         end_value=ion_minus_att;   %Save end value
      elseif rem(m,2)==0
         evens=evens+ion_minus_att; %Sum even values
      else odds=odds+ion_minus_att; %Sum odd values
      end
   end
   N=exp(dr/3*(start_value+2*evens+4*odds+end_value)); %exp(Simpson's
integration rule)
end
Gcond(11,1)=V/(rc*log(R/rc));
```

```
%Display the results
disp([' '])
disp(['Results'])
disp(['======='])
disp(['Peek                 : ' ,num2str(Gcond(1,1)),'kV/cm'])
disp(['Whitehead (+ve)      : ' ,num2str(Gcond(2,1)),'kV/cm'])
disp(['Whitehead (-ve)      : ' ,num2str(Gcond(3,1)),'kV/cm'])
disp(['Heymann (min)        : ' ,num2str(Gcond(4,1)),'kV/cm'])
disp(['Heymann (max)        : ' ,num2str(Gcond(5,1)),'kV/cm'])
disp(['Khalifa (+ve, min) : ' ,num2str(Gcond(6,1)),'kV/cm'])
disp(['Khalifa (+ve, max) : ' ,num2str(Gcond(7,1)),'kV/cm'])
disp(['Khalifa (-ve, min) : ' ,num2str(Gcond(8,1)),'kV/cm'])
disp(['Khalifa (-ve, max) : ' ,num2str(Gcond(9,1)),'kV/cm'])
disp(['Zaengl               : ' ,num2str(Gcond(10,1)),'kV/cm'])
disp(['WSU Onset Criterion: ' ,num2str(Gcond(11,1)),'kV/cm'])
disp(['===================================================='])

%Save the results to a file
fopen('d:\eamon\UDW_MSc\matlabstuff\smooth_cond_surface_stress.txt');
dlmwrite('d:\eamon\UDW_MSc\matlabstuff\smooth_cond_surface_stress.txt',Gcond,'\t
');
fclose('all');
```